Please cite this article in press as: Issa et al., Multiscale Optical Ca^{2+} Imaging of Tonal Organization in Mouse Auditory Cortex, Neuron (2014), http://dx.doi.org/10.1016/j.neuron.2014.07.009

Neuron
Article

Multiscale Optical Ca^{2+} Imaging of Tonal Organization in Mouse Auditory Cortex

John B. Issa,[1] Benjamin D. Haeffele,[1] Amit Agarwal,[3] Dwight E. Bergles,[3] Eric D. Young,[1,3] and David T. Yue[1,2,3,*]
[1]Department of Biomedical Engineering
[2]Center for Cell Dynamics
[3]Solomon H. Snyder Department of Neuroscience
The Johns Hopkins University School of Medicine, Baltimore, MD 21205, USA
*Correspondence: dyue@jhmi.edu
http://dx.doi.org/10.1016/j.neuron.2014.07.009

SUMMARY

Spatial patterns of functional organization, resolved by microelectrode mapping, comprise a core principle of sensory cortices. In auditory cortex, however, recent two-photon Ca^{2+} imaging challenges this precept, as the traditional tonotopic arrangement appears weakly organized at the level of individual neurons. To resolve this fundamental ambiguity about the organization of auditory cortex, we developed multiscale optical Ca^{2+} imaging of unanesthetized GCaMP transgenic mice. Single-neuron activity monitored by two-photon imaging was precisely registered to large-scale cortical maps provided by transcranial widefield imaging. Neurons in the primary field responded well to tones; neighboring neurons were appreciably cotuned, and preferred frequencies adhered tightly to a tonotopic axis. By contrast, nearby secondary-field neurons exhibited heterogeneous tuning. The multiscale imaging approach also readily localized vocalization regions and neurons. Altogether, these findings cohere electrode and two-photon perspectives, resolve new features of auditory cortex, and offer a promising approach generalizable to any cortical area.

INTRODUCTION

The functional organization of primary sensory cortices (e.g., visual, somatosensory, and auditory) often mirrors the spatial organization of their peripheral sensing organs (Kaas, 1997, 2011). The resulting functional maps of cortex have proven invaluable, both to compare recording locations across experiments and to track an operational correlate of synaptic plasticity (Buonomano and Merzenich, 1998; de Villers-Sidani et al., 2008; Guo et al., 2012; Karmarkar and Dan, 2006). Nonetheless, the supporting data for these maps have often drawn from methods that average activity across multiple neurons; thus, the extent to which these canonical maps pertain to individual neurons remains to be determined.

In particular, these maps have traditionally been resolved by extracellular electrode recordings, densely sampled across a large cortical area with accurate spike detection. Alternatively, a complementary view has come from widefield optical imaging that simultaneously surveys expansive cortical regions. For instance, to gauge neural tissue activity, these approaches monitor local changes in blood flow or altered flavoprotein oxidation (Honma et al., 2013; Takahashi et al., 2006); alternatively, regions of depolarization may be directly detected via voltage-sensitive dyes bulk loaded into neuropil (Grinvald and Hildesheim, 2004). While these spatially expansive approaches provide holistic global maps, they are often limited by low signal fidelity and spatial resolution. Most recently, two-photon Ca^{2+} imaging has promised major advances at an intermediate scale, enabling simultaneous monitoring of large numbers of neurons within a local region (Andermann et al., 2011; Ohki et al., 2005; Svoboda and Yasuda, 2006). This approach has the potential to expand our knowledge of the functional organization of cortex.

For auditory cortex, however, paradoxical observations have emerged between methods. Electrode recordings consistently substantiate a cochleotopic organization. This arrangement—also referred to as spectral organization or tonotopy—originates from the base-to-apex selectivity of the cochlea for decreasing frequencies of incoming sound (Pickles, 2012). This spectral organization is subsequently maintained through much of the auditory system (Hackett et al., 2011; Kaas, 2011). In mouse cortex, the primary auditory fields (primary auditory cortex [AI] and anterior auditory field [AAF]) contain best-frequency spatial gradients (tonotopic axes) that mirror each other (Guo et al., 2012; Hackett et al., 2011; Joachimsthaler et al., 2014; Stiebler et al., 1997). Other auditory fields are less well-characterized; these include the ultrasonic field (UF), which responds to high-frequency sounds and may be an extension of dorsorostral AI (Guo et al., 2012), and the secondary auditory field (AII), which sits ventral to the primary fields and may not be spectrally organized (Stiebler et al., 1997). Instead, AII has been theorized to support higher-order novelty and sound-object processing (Geissler and Ehret, 2004; Joachimsthaler et al., 2014).

By contrast, recent two-photon Ca^{2+} imaging of individual neurons in AI and AAF, using Ca^{2+}-sensitive dyes bulk loaded into tissue, paints a different picture. Tuning of individual neurons is often poor, with only weak responsiveness over a broad frequency range. Moreover, frequency tuning of neighboring neurons (<100–200 μm apart) is largely uncorrelated, with best

frequencies varying by up to three to four octaves (Bandyopadhyay et al., 2010; Chen et al., 2011; Rothschild et al., 2010). Finally, an overall tonotopic axis that spans AI is only negligibly (Bandyopadhyay et al., 2010) or inconsistently (Rothschild et al., 2010) resolved over larger distances, with strikingly poorer correlations observed between preferred frequency and position along a tonotopic axis compared to microelectrode studies (Table S1 available online). This discord—between the strong tonotopy observed over decades of electrode recordings versus the diverse and weak tonal selectivity measured with two-photon Ca^{2+} imaging—presents a key hurdle to leveraging the two-photon approach to define cortical circuits and raises questions about the spectral organization of auditory cortex (Guo et al., 2012), particularly as it relates to experience-dependent plasticity of tonotopic maps (de Villers-Sidani and Merzenich, 2011). Potential explanations include actual differences in the neurons interrogated by the two techniques, effects of anesthesia that disproportionately mute signal detection by Ca^{2+} imaging (Wang, 2007), or inadvertent two-photon imaging of regions outside intended loci.

We therefore develop a preparation that enables two-photon Ca^{2+} imaging of mouse auditory cortex in unanesthetized mice to preserve cortical activity. Also crucial is our use of a transgenic mouse in which neuronal expression of the genetically encoded Ca^{2+} indicator GCaMP3 is controlled by the Cre-Lox system (Tian et al., 2009; Zariwala et al., 2012). This approach furnishes widespread expression of GCaMP3 in a manner reproducible across cortices and mice, aiding comparison across large sectors of auditory cortex. Of equal importance, we discover that GCaMP3-expressing mice permit robust transcranial widefield imaging of auditory cortical activity, allowing resolution of a global functional map before undertaking two-photon Ca^{2+} imaging to interrogate individual neurons. These global maps can be delineated from only a single-trial set of tone presentations, enabling rapid registration of individual neurons to their precise locations within a global map. With these advances, we reconcile the conflicting perspectives on tonotopicity of AI, shed light on the organizational features of AII, and identify vocalization-responsive regions and neurons. Our approach—Ca^{2+} imaging across multiple spatial scales in functional mapping experiments—may be generalized for studying coding and functional organization in any sensory cortex.

RESULTS

GCaMP-Based Transcranial Functional Imaging

We sought a convenient method for macroscopic mapping of auditory cortex, a strategy that would allow rapid and definitive subsequent registration of individual neurons interrogated under in vivo two-photon Ca^{2+} imaging. For this purpose, we utilized unanesthetized transgenic mice expressing GCaMP3 in neurons (Syn1-Cre; R26-lsl-GCaMP3 or Emx1-Cre; R26-lsl-GCaMP3) (Zariwala et al., 2012). Using immunohistochemistry and Ca^{2+} imaging, we verified that GCaMP3 expression was predominantly in neurons rather than in glia (Figures S1 and S7A–S7C). After exposing and thinning the skull overlying left auditory cortex, we performed widefield epifluorescence imaging on restrained, head-fixed mice (Figure 1A). The baseline fluorescence "scout" image shows the overall field, which spans a ~4 mm^2 area (Figure 1B). Blood vessels are clearly resolved in black, which serve as useful guides for subsequent registration. In response to sinusoidal amplitude modulated (SAM) tones delivered to the right ear, we routinely resolved single-trial fluorescence responses of sizeable magnitude (~5% $\Delta F/F_O$ with SD ~0.3% $\Delta F/F_O$; metrics averaged from three mice). This profile grants signal-to-noise ratios of ~15 (Figures 1C and S2A–S2C) and SDs of ~1% across trials (Figure S2D). The fluorescence signals displayed in the upper rows of Figure 1C correspond to the three regions marked in Figure 1B, and the affiliated tone presentations are registered below by blips. For comparison, we also considered the use of an established approach to transcranial macroscopic imaging based on flavoprotein fluorescence (Takahashi et al., 2006). Our own attempts at such imaging yielded transients of ~0.1% $\Delta F/F_O$ and a signal-to-noise ratio of ~1 (data not shown). Thus, GCaMP3-based imaging represented a crucial enabling advantage for the present study.

We next investigated the spatial organization of these signals. Indeed, responses to different tone frequencies were spatially distinct in the same mouse (Figures 1D, S2E, and S2F). In particular, low-frequency stimuli elicited spatially restricted responses in the three regions ("poles") within the leftmost subpanel of Figure 1D (labeled "L"). By contrast, high-frequency sounds elicited responses in four different poles, labeled "H" in the rightmost subpanel of Figure 1D. As might be expected, tone presentation of middle frequencies evoked peak responses at intermediate positions (Figure 1D, middle subpanel). As the locations of these "L" and "H" poles were largely consistent across different sound levels and tone durations (Figure S3), we used the local center of mass of pole activities as landmarks for subsequent registration of two-photon imaging fields. Details on forming these transcranial signals and images (Figures 1C and 1D) are described in Supplemental Experimental Procedures (Transcranial Image Analysis) and Figure S2.

To form a detailed spatial map of spectral tuning from such images, we calculated a preferred frequency at each pixel. First, we recorded response images across a range of sound levels and frequencies as shown by the thumbnail image collage in Figure 2A. The images were processed as in Figure 1D but are shown with an inverted grayscale format for clarity at reduced display size. Sound attenuation is graded along the y axis and frequency along the x axis. Second, based on these responses, we selected the weakest sound level that elicited a response for the field as a whole, yielding the jagged border line in Figure 2A. Reassuringly, this estimate of cortical threshold versus frequency accords well with other measures of hearing thresholds in C57BL/6 mice (Mikaelian et al., 1974; Taberner and Liberman, 2005) (Figure S4A). Third, at each pixel, a weighted average of the frequencies eliciting the largest responses provided an estimate of the preferred frequency. For visualizing these tuning preferences, we formed the map shown in Figure 2B, where hue indicates preferred frequency and color saturation indicates response strength. Weakly responsive regions appear as white pixels. As expected, this detailed map (Figure 2B) agrees well with the landmarks chosen for low- and high-frequency stimuli (Figure 1D). Importantly, transcranial maps could be reproducibly obtained across mice (Figure 2C), as shown by maps from

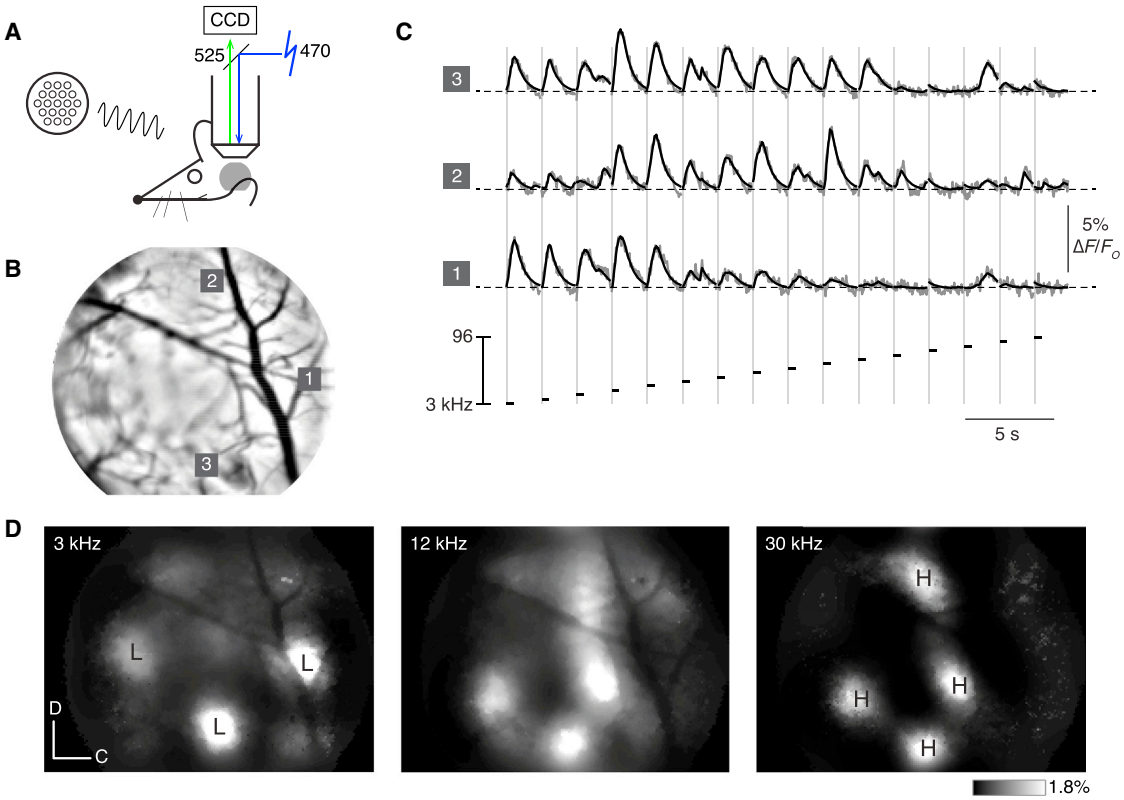

Figure 1. Transcranial Responses to SAM Tones in GCaMP3 Mice

(A) Transcranial Ca^{2+} imaging layout. Speaker emits sinusoidal amplitude-modulated (SAM) tones to right ear of head-fixed, unanesthetized mouse. The 470 nm excitation illuminates thinned skull over left auditory cortex (gray circle). The 525 nm emission collected by CCD camera.

(B) Average transcranial fluorescence image from exemplar mouse, expressing GCaMP3 under Emx1-Cre driver line. Vasculature landmarks are low signal.

(C) Ca^{2+} activity induced by SAM tones at three regions marked in (B). Upper three rows, single-trial fluorescence responses. SAM tones delivered every 2 s, covering a five-octave range in random order. For convenience, traces here sorted by increasing frequency, as labeled on bottom. Original baseline-corrected signal in gray and sparse-encoding waveform in black.

(D) Ca^{2+} activity over entire auditory region during presentation of low-, middle-, and high-frequency tones. Images displayed in grayscale format (equivalent $\Delta F/F_O$ scale bar, lower right) after processing by sparse-encoding algorithm and deblurring. Loci of strongest response to low (L) and high (H) frequency tones marked on 3 and 30 kHz images, respectively. Dorsal-caudal spatial scale bar on lower left denotes 300 μm along each dimension.

(B–D) Data from same mouse.

two other mice (M2 and M7). After adjusting for differences in landmark positions between mice via elastic registration (Figure S5), averaging seven maps yielded a canonical arrangement (Figure 2D). The resemblance of this meta configuration to that of individual mice (Figures 2B and 2C) substantiates the reproducibility of maps across mice.

This reproducibility allowed for analysis of additional features of spectral organization (Figure 2E, corresponding to the merged field in Figure 2D). In particular, we resolved four low-to-high frequency gradients, depicted as thick black L→H trajectories in Figure 2E, where each gradient is here defined by the trajectory of local maxima of Ca^{2+} activity with increasing tone frequency (Figure S4). These gradients and the high- and low-frequency poles permitted identification of the likely locations of AI/UF, AAF, and AII (Figure 2F), as follows. For AI, two gradients traveled rostrally. The dorsal branch terminated in UF, consistent with recent extensive microelectrode mapping (Guo et al., 2012). The ventral branch moved toward AII and this outcome was a robust and characteristic feature in mice. For AAF, the traditional tonotopic axis defined by microelectrode mapping would extend from the low-frequency pole in AAF to the high-frequency pole in UF (Guo et al., 2012), as depicted by the dashed arrow connecting AAF "L" with UF "H" in Figure 2F. Importantly, however, the traditional gradient traces a path tracking the steepest rate of change in preferred frequency with distance (Guo et al., 2012), regardless of comparative response strength. If we were to use a similar definition, this tone axis would be present in our data along the dashed arrow in Figure 2F. However, we often observed comparatively weak responsiveness along this path. Accordingly, for purposes of robust fiducial orientation, we favored calculation of the ventrally directed L→H gradient in AAF (Figures 2E and 2F), which tracks local maxima of response strength. Reassuringly, this ventrally directed gradient concurs with results from intrinsic imaging methods (Honma et al., 2013). Finally, for AII, the robust activity we monitor under transcranial Ca^{2+} imaging enabled observation of a dorsoventral

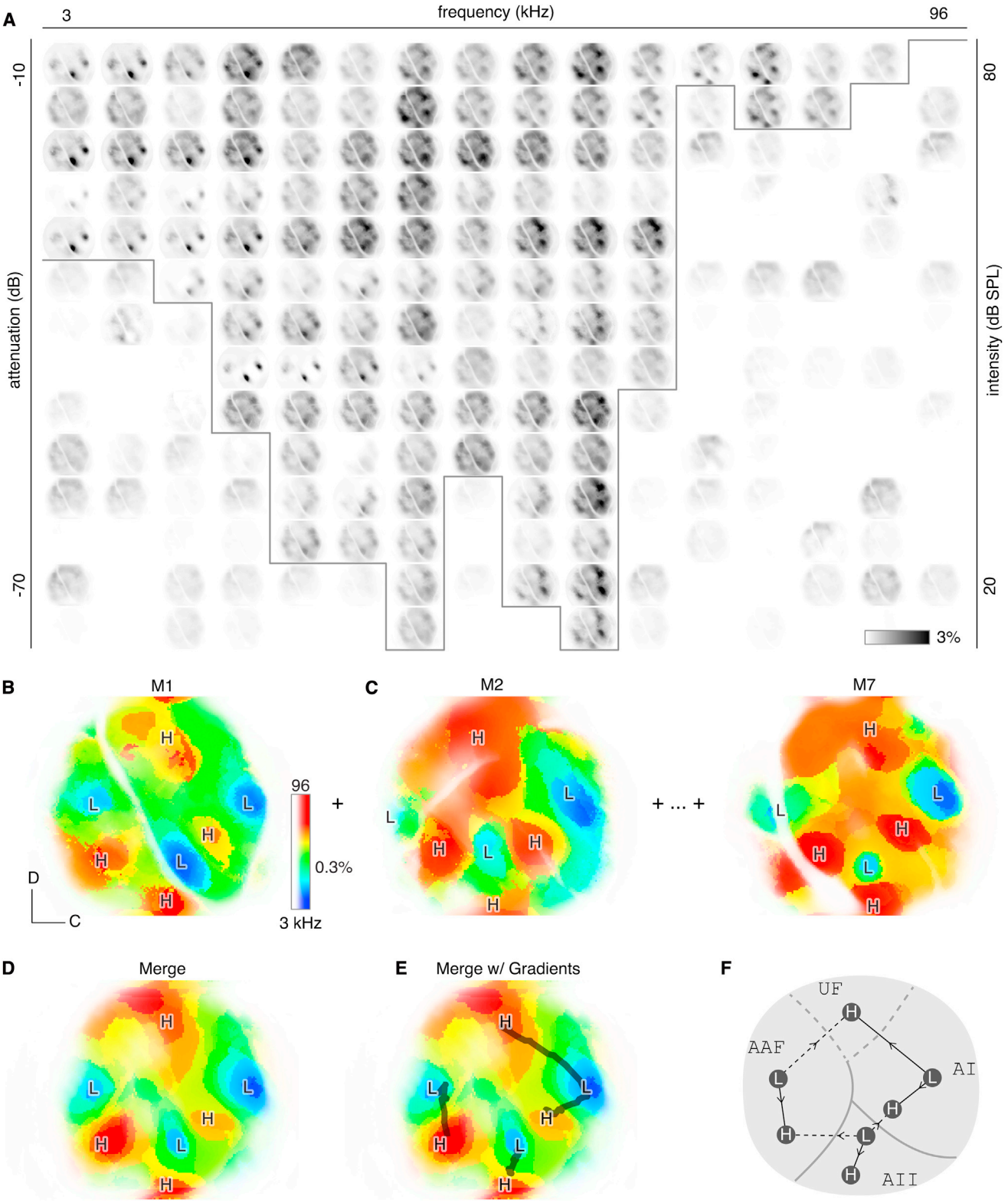

Figure 2. Formation of Transcranial Map of Auditory Cortices

(A) Single-trial transcranial fluorescence responses during SAM tones of various frequencies (x axis) and sound attenuations (y axis, left). SPL intensities, y axis on right, coarsely corrected for speaker calibration. Images as in Figure 1D, but plotted as inverted grayscale format (equivalent $\Delta F/F_O$ scale bar, lower right).

(legend continued on next page)

gradient (Figures 2E and 2F), a feature not previously discerned in electrode studies using anesthesia (Guo et al., 2012).

Ca^{2+} Responses of Individual Neurons Registered to AI

Following acquisition of a global transcranial activity map, we performed a craniotomy over the left auditory cortex and undertook two-photon Ca^{2+} imaging of individual neurons at depths of 150 to 430 μm (Figure S1Q), with most neurons residing within layers II/III. Figure 3 displays the results for a single exemplar neuron. Figure 3A outlines the registration of this neuron to the low-frequency pole of AI. The transcranial map for this mouse is displayed in the left subpanel, and the relevant two-photon field is shown in the middle subpanel (exemplar neuron boxed). SAM tone presentation at a preferred frequency produced a substantial increase in fluorescence over that observed in quiescent periods (respective bottom and top images in rightmost subpanels). Figure 3B displays a single-trial fluorescence trace of this same neuron during presentation of randomly ordered SAM tones (−20 dB sound attenuation) with frequencies denoted below the trace. This record exhibits sizeable responses to low-frequency stimuli (Figure S6), allowing reliable discrimination of tuning characteristics. Upon sorting traces by increasing stimulus frequencies and averaging across multiple trials, the sharply tuned response preference of this neuron for low-frequency tones is evident (Figure 3C, top row). Individual trial responses are shown in gray, and the average response overlaid in black. At weaker sound levels (Figure 3C, middle and bottom rows), responses become smaller and more selectively tuned. The frequency-response area (FRA) of this neuron (Figure 3D) highlights its monotonic level dependence and preference for low-frequency tones. To improve resolution, FRAs were deduced from deconvolved and thresholded signals, here and throughout (Figure S6; Supplemental Experimental Procedures [Two-Photon Image Analysis]). Across all active GCaMP3 neurons in our study, single events detected by deconvolution and thresholding had mean amplitudes of ∼6% ± 1.5% $\Delta F/F_O$ (mean ±SD) and decay time constants of ∼0.8 s (Figures S7A–S7C). These outcomes are similar to single-spike transients in a prior study of in vivo GCaMP3 activity (Tian et al., 2009).

While this exemplar neuron exhibits sharp tuning to low-frequency tones, what about neighboring neurons in the same field (Figures 4A–4C)? For reference, Figure 4A again registers the location of the exemplar two-photon field to the low-frequency pole in AI, with a slightly larger fluorescence "scout" image of the two-photon field shown on the bottom. The field contains 47 neurons that could be detected based on expressed GCaMP3 fluorescence, 53% of which showed fluorescence transients at any point. Of those, 80% were found to be responsive to tones, where the colored circles indicate the best frequency (*BF*) of these tone-responsive neurons. Across all fields in this study, 835/1,407 fluorescent neurons exhibited Ca^{2+} transients ("active" neurons), and 297 of these active neurons (36%) responded to tones ("tone-responsive" neurons). Figure 4B displays the frequency response characteristics of five of these tone-responsive neurons from the field in Figure 4A. The average responses to SAM tones (−20 dB attenuation) are plotted in the left column, using the same format as Figure 3C (top row). FRAs for these neurons are displayed in the right column, using identical procedures to those in Figure 3D (cell 3 is the same as in Figure 3). A first notable result is that some variability exists between neurons; thus, these signals reflect the activity of individual neurons rather than whole-field neuropil contamination (a concern with bulk loading of chemical-fluorescent Ca^{2+} dyes) (Kerr et al., 2005). Second, despite modest variability, all five neurons clearly responded within a one-octave low-frequency range.

In fact, population analysis across the entire field (all circled neurons in Figure 4A) corroborated and extended these trends, as detailed in Figure 4C. The topmost subpanel shows the average FRA for the entire field, demonstrating sharp, low-frequency tuning across the population. Note the similarity to the FRA from the individual neuron shown in Figure 3D. The middle subpanel summarizes population data describing the spread in best frequencies across the field, quantified as "BF spread" (Δ*BF*). This metric tallies the difference in best frequencies between each pair of tone-responsive neurons in the field, in octaves. Specifically, the sharp rise of the cumulative histogram for Δ*BF* shown here, corresponding to a mean value of 0.258 octaves, substantiates that neurons across this field are highly cotuned to a similar preferred frequency. Additionally, the bottom subpanel displays population data for the sharpness of tuning across the field, as gauged by a *Q* factor defined as the *BF* divided by the bandwidth of responsiveness. The sharp rise of the cumulative histogram of *Q*, affiliated with a large mean value of 2.26, argues that neurons across the field are well tuned.

The remainder of the figure summarizes results for two-photon fields registered to middle- (Figures 4D–4F) and high-frequency

Jagged, thin black line indicates approximate threshold, lowest sound level eliciting responses at given frequency. Signals below threshold reflect spontaneous activity. Mouse expressing GCaMP3 under Syn1-Cre driver line.

(B) Best-frequency map for the same experiment. Each pixel plots a color map readout of weighted average of three frequencies eliciting largest responses at threshold sound level. Color map (lower right) associates best frequencies (y axis) with specific colors (e.g., blue = low; red = high); color saturation (x axis) denotes strength of best-frequency responses. Low- and high-frequency hotspots (L and H labels, respectively), determined as local center of mass coordinates calculated over low- and high-frequency islands, serve as landmarks throughout. Dorsal-caudal spatial scale bar on lower left denotes 300 μm along each dimension.

(C) Transcranial response maps as in (B) for two other mice (M2 and M7). Slight differences exist in colors and precise layout of landmarks, but overall features and low-to-high frequency gradients are preserved. Mice expressing GCaMP3 under Emx1-Cre (M2) and Syn1-Cre (M7).

(D) Average of seven transcranial response maps, including those in (B) and (C), demonstrating conserved canonical layout across mice. Landmark-based registration morphs each individual map onto a common coordinate system before averaging (see Figure S5).

(E) Global map from (B), with dark-thick-line paths of maximally responsive loci (local center-of-mass) with increasing frequencies. Trajectories derived from solid arrows in (F).

(F) Coarse schematic of mouse auditory cortex, from transcranial imaging of mouse M1. Solid lines with arrows, best fits to data; dashed lines with arrows, poorer fits. Details in Figure S4.

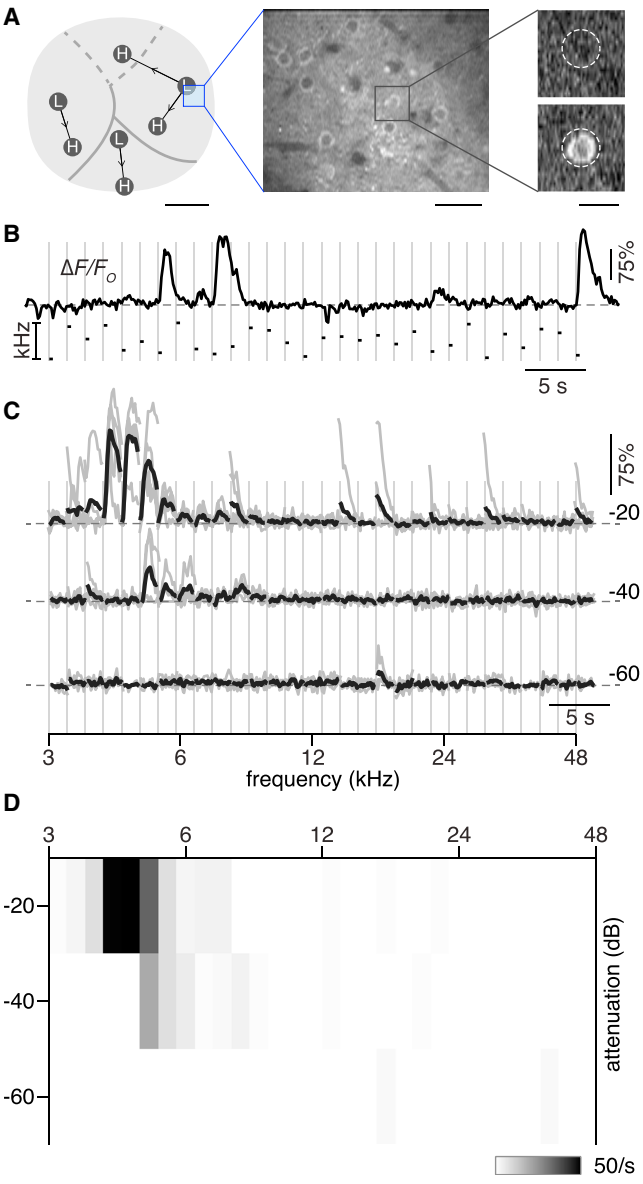

Figure 3. Tonal Tuning of Exemplar Neuron Residing within Low-Frequency Pole of AI

(A) Registration of neuron to transcranial map. Left subpanel, high- (H) and low-frequency (L) landmarks obtained via transcranial imaging (scale bar, 500 μm). Box registers overall field of view for neuron-by-neuron imaging under two-photon microscopy. Middle subpanel, portion of actual field of view acquired under scanning two-photon microscopy (scale bar, 30 μm) reporting time-averaged fluorescence. Box registers individual neuron to be scrutinized in right subpanel. Right subpanel, change in fluorescence of this neuron between quiet (top) and active (bottom) periods (scale bar, 10 μm). GCaMP3 under Syn1-Cre driver line.

(B) Single-trial fluorescence as a function of time from neuron in (A) (right subpanel). Time-registered blips show frequency and timing of 30 randomly delivered SAM tones logarithmically spaced between 3 and 48 kHz.

(C) Fluorescence responses from same neuron, after sorting for tone presentation in order of increasing frequency (left to right). Each row relates to stimuli presented at different levels of sound attenuation. Results of individual trials plotted in gray and averaged responses across multiple trials in black. Strong and sharp tuning to low frequencies of 4 to 5 kHz.

(D) FRA for this neuron, confirming low-frequency tuning. Intensity displays estimated spike rate, gauged by deconvolving and thresholding traces (Figure S7).

(Figures 4G–4I) loci of AI in the global transcranial map. For these other regions, we also observed clustered tuning among nearby neurons, appropriately tuned to middle- and high-frequency tones. Further, each neuron had responses to a limited range of frequencies. Thus, strong cotuning and narrow spectral preference seem characteristic across AI. Finally, the frequency preference of individual neurons in these low-, middle-, and high-frequency exemplar fields adheres to tonotopic organization expected from transcranial maps (e.g., see average FRAs in Figures 4C, 4F, and 4I). Further data and analysis substantiating these trends will be presented after characterization of fields in AII.

Ca^{2+} Responses of Individual Neurons Registered to AII

Beyond AI, our method allowed unambiguous identification of single-neuron responses in other auditory areas that have received comparatively little attention in prior two-photon Ca^{2+} imaging studies. In particular, we focused on AII. On the basis of multiunit electrode recordings, neurons in AII may exhibit broad and multipeaked tonal tuning (Stiebler et al., 1997). However, these multiunit records leave open the possibility that the observed broad tuning actually reflects summation of sharply but heterogeneously tuned individual neurons.

Figure 5 presents the results for three two-photon fields registered to AII, displayed according to the format in Figure 4. These fields progress along the AII dorsoventral axis identified earlier in transcranial maps (Figure 2D). The low frequency pole ("L") is situated at the dorsal end of this axis and the high frequency pole ("H") at the ventral end. Results for a field registered to the "L" pole are displayed in Figures 5A–5C, those for an intermediate point along the axis are shown in Figures 5D–5F, and those for the "H" pole are shown in Figures 5G–5I. These exemplar fields illustrate notable similarities and sharp contrasts in relation to AI. First, large tone-responsive Ca^{2+} signals could be resolved for individual neurons throughout AII, with response amplitude at least equivalent to that in AI (Figures 5B, 5E, and 5H). Second, while clearly tone responsive, many of these neurons were activated by tones spanning a remarkably broad frequency range. For example, for both neuron 3 in Figure 5B and neuron 4 in Figure 5E, strong responses were well maintained over a two to three octave range, something not observed in AI. This broadness of tuning is reflected in the expansive width of some of the single-neuron FRAs (right end of Figures 5B, 5E, and 5H) and by cumulative population histograms demonstrating lower sharpness-of-tuning *Q* values (Figures 5C and 5F). Third, best frequencies among neighboring neurons could widely diverge, particularly as illustrated by the mid-frequency field. Here, neurons in the field collectively respond well to tones spanning the entire five-octave test range (Figure 5E), and the cumulative histogram for ΔBF is impressively right shifted (Figures 5F). Fourth, both the broad tuning of individual neurons and dispersion of best frequencies within fields collectively produced appreciable widening of whole-field average FRAs relating to all AII exemplar fields (Figures 5C, 5F, and 5I). This profile clearly contrasts with

average FRAs measured in AI (Figures 4C, 4F, and 4I). Finally, despite the broad and diverse tuning of AII fields, there was some correspondence between field location and preferred frequencies. The most dorsal "L" field tended to respond to low frequencies (Figure 5C, average FRA), and the most ventral "H" field preferred higher frequencies (Figure 5I, average FRA). This outcome rationalizes the coarse AII tone gradient observed under transcranial mapping.

Functional Organization of AI and AII Cortices Revealed by Multiscale Optical Ca^{2+} Imaging

The results from exemplar AI and AII fields presented thus far hint at the existence of fundamental contrasts in the functional organization of AI and AII auditory subregions. Importantly, the use of transgenic GCaMP3 mice to interrogate individual neurons registered to transcranial maps facilitated the characterization of numerous other fields, drawn from a total of 22 mice. Thirteen fields were investigated in total along the axis extending from the low-to-high frequency AI poles, as denoted in Figure 6A by squares within the translucent-cyan ovoid. Sixteen fields were studied in total along the AII low-to-high frequency axis, as marked in Figure 6D by squares within the translucent-yellow ovoid. The analysis here included all neurons whose activity increased with any tone presentation, regardless of frequency preference or tuning (see Suplemental Experimental Procedures [Response Metrics]). This large data set fully established the trends observed above in exemplar fields. To test for a strong tonotopic axial organization in AI, we plotted best frequencies of all 154 tone-responsive neurons in these fields versus their position along a normalized axis coordinate (Figure 6B, black-filled symbols), where "0" denotes the low-frequency AI pole and "1" marks the dorsal high-frequency AI pole. Precise coordinates were determined by orthogonal projection onto the ventrodorsal, low-to-high-frequency axis of AI, as determined in individual mice. Additionally, the mean *BF* and coordinate position for fields were plotted on the same axis (Figure 6B, translucent squares). Both of these plots substantiate an excellent linear fit to all the two-photon data (Figure 6B; $r = 0.88$, $p < 0.001$ via Pearson's analysis of 154 neurons), indicating that AI has a well-resolved tonotopic organization. Still, one remaining ambiguity might be that, while this relation is evident when compiled from multiple fields across the entire AI tonotopic axis (Figure 6B, black symbols), this trend is not obvious within individual fields of sizes <250 μm (as seen with our usual 40× objective). However, data-based simulations predicted that computed linear correlations would yield *r* values >0.5 only if field sizes were >300 μm (Figure S8A). Reassuringly, a linear trend was then clearly resolved within a single larger field (375 μm) imaged with a 25× objective (Figures 6B, red symbols, and S8B–S8D; $r = 0.66$ and $p < 0.001$ via Pearson's analysis of 30 neurons). In further support of tonotopy, cumulative histograms incorporating results from all 40× fields demonstrated limited Δ*BF*, indicative of strong cotuning among neighboring neurons (Figure 6C, top; dashed vertical line and symbol mark the mean). Moreover, cumulative histogram analysis of *Q* factors corroborates sharp frequency tuning within individual neurons throughout AI (Figure 6C, bottom; dashed vertical line and symbol mark the mean). These *Q* values are similar to those found by microelectrode methods in rodent auditory cortex (Polley et al., 2007).

In contrast, the same analysis applied to the large data set for AII indicates a substantially different profile. Contrary to prior expectations, we indeed resolve a weaker though significant tonotopic organization within AII, with adherence of *BF* to a tonotopic axis (Figure 6E) yielding a linear correlation with $r = 0.54$ ($p < 0.001$ via Pearson's analysis of 143 neurons). Population statistics for Δ*BF* and *Q* in Figure 6F indicate that cotuning and sharpness of tuning within local neuronal subpopulations in AII differ significantly from those in AI. In particular, we observe significantly decreased cotuning of neighboring neurons compared to AI (Figure 6F, top; $p < 0.042$, two-sided Mann Whitney) and far broader frequency tuning within individual neurons (Figure 6F, bottom; $p < 0.02$, two-sided Mann Whitney). In Figure 6F, AII data are plotted in black with fits to AI data reproduced in gray for reference. To account for any potential influence of different-sized fields on the use of Δ*BF* to compare cotuning among neighboring neurons, we also normalized this metric by the distance *d* between pairs of neurons. This approach also furnished significantly different Δ*BF*/*d* values of 0.008 ± 0.005 octaves/μm for AI (mean ±SD) versus 0.0149 ± 0.01 octaves/μm for AII ($p < 0.032$, two-sided Mann Whitney, performed on metrics from 13 AI versus 16 AII fields). All these population comparisons thereby substantiate that neurons in AII are not only more broadly tuned than neurons in AI but also more disparately tuned from their neighbors (Figures 6D–6F). Though many of these features are newly recognized, the larger *Q* values we observe are similar to those observed by microelectrode recordings in a potentially comparable rodent ventral auditory field (Polley et al., 2007).

Overall then, within the primary fields (AI and AAF), there is considerable agreement between the tonotopic functional organization established here by Ca^{2+} imaging and that resolved previously via microelectrode mapping. Notably, high- and low-frequency poles of our global transcranial map (from Figure 2B) overlay well onto a recently published microelectrode layout reproduced in Figure 7A (Guo et al., 2012). By contrast, in AII, we newly resolve a significant, though weaker, tonotopic scheme (Figures 2E and 6D–6F). Additionally, in AAF, a ventrally directed gradient (Figure 2E; and Figure 7B, red arrow), identified by tracking maximal activity with increasing tone frequencies, differs from the traditional axis shown as a dashed blue arrow in Figure 7B (Guo et al., 2012). This discrepancy may occur because the customary gradient traces the steepest rate of change in *BF*. The two definitions often yield identical axes (e.g., dorsally directed AI axis shown by green arrow in Figure 7B), but for AAF, new organizational features may emerge.

Responses to Complex Stimuli Identified by Multiscale Approach

We next tested whether our multiscale approach could identify cortex specialized for more complex stimuli. Under transcranial imaging, we typically observed a region encompassing the border of AI and AAF that was only sparingly responsive to tones, which is visualized by taking the average fluorescence response to SAM tones over all frequencies, with tones delivered at the highest sound level tested (Figure 7C, left subpanel). The darker zone in the dashed oval is intriguing because adult mouse

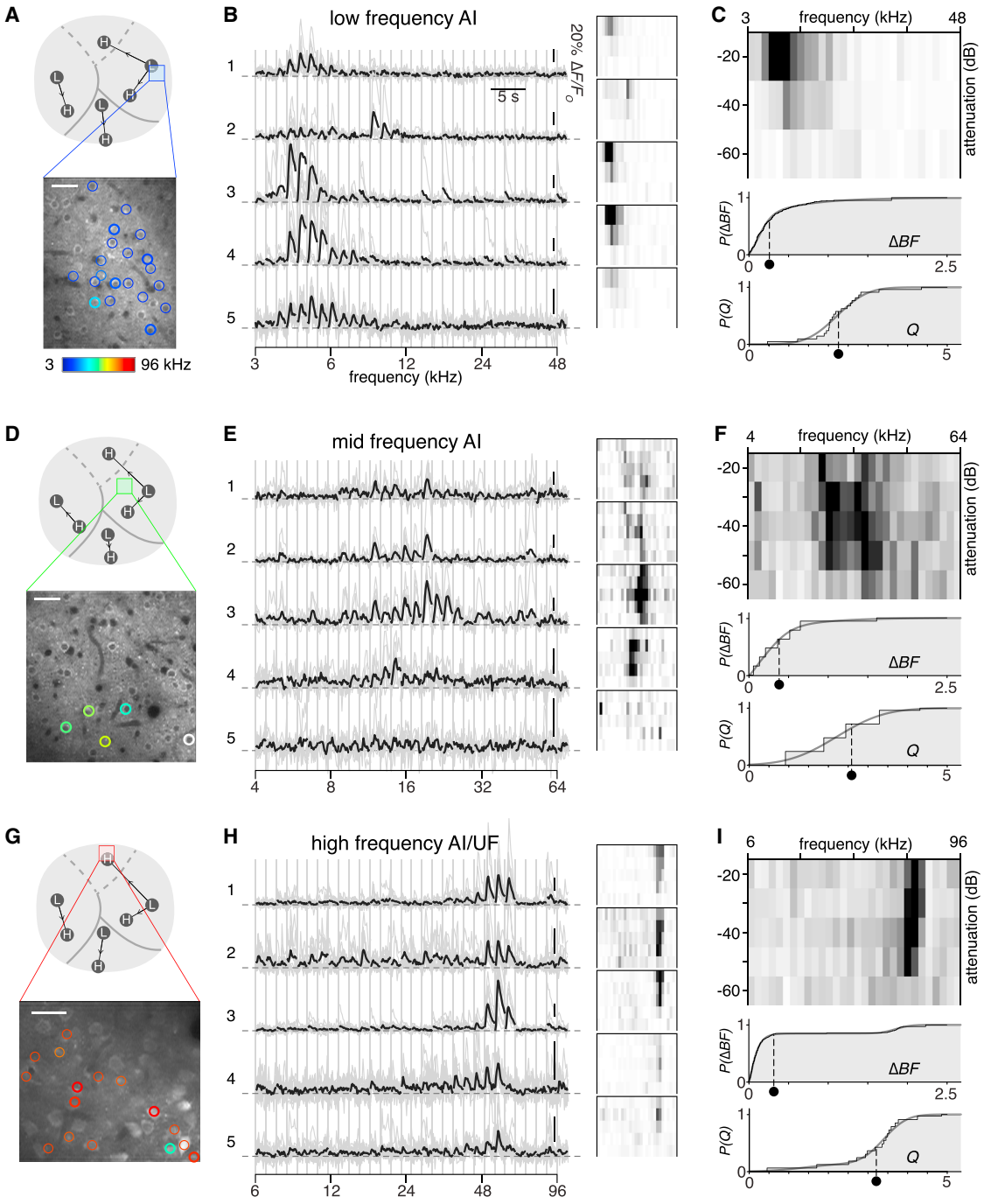

Figure 4. Spatially Colocalized AI Neurons Show Sharp Tuning to Similar Tone Frequencies

(A–C) Neuron-by-neuron responses in low-frequency AI, encompassing same field as Figure 3. GCaMP3 under Syn1-Cre.

(A) Landmarks from transcranial imaging, with registered two-photon imaging field. Same field and format as in Figure 3A, but two-photon field here encompasses modestly larger region (scale bar, 30 μm). Colored circles, *BF* of sound-responsive neurons, with color map at bottom (blue = low frequency, red = high frequency). Thicker circles delineate neurons whose responses appear in (B).

(B) Activity of five neurons marked in (A); format as in Figure 3C. Neuron 3 is same as shown in Figure 3. Sound attenuation of −20 dB was used throughout (B) and (H). FRAs on right follow format in Figure 3D. FRAs scaled to 24.6 events/s.

(C) Top subpanel, FRA averaged from all active neurons in entire field showing considerable population tuning to low frequency stimuli. Scaled to 5.64 events/s. Middle subpanel, cumulative distribution of Δ*BF* (in octaves here and throughout) between all pairs of tuned neurons in field. Bottom subpanel, cumulative distribution of sharpness of tuning metric (*Q* factor) for all tone-responsive neurons in field, substantiating narrow frequency preference within individual neurons. Vertical dashed lines and symbols delineate mean values.

(legend continued on next page)

vocalizations (Grimsley et al., 2011) presented to this same mouse nicely elicit responses extending into the oval (Figure 7C, right subpanel). Taking the ratio of vocalization to tone responses highlights the difference (Figure 7D), as green regions correspond to pixels favoring vocalization, which overlap heavily with the region insensitive to tones (dashed oval reproduced from Figure 7C). Blue regions denote pixels favoring tones.

Next, we investigated the response properties of single neurons within vocalization-selective regions. A set of ten mouse vocalizations were used, of which nine contained energy only in the ultrasonic range as illustrated by their spectrograms (Figure 8A). After identifying a tone-insensitive region via transcranial Ca^{2+} imaging (magenta oval, Figure 8B, left subpanel), we intentionally focused on a presumed high-frequency AAF region (marked by a rectangle) that corresponded to a border between vocalization-preferring (green) and tone-preferring (blue) sectors (Figure 8B, middle subpanel). The right subpanel displays the corresponding two-photon field at this location. Responses to vocalizations (Figure 8C) and SAM tones (Figure 8D) under two-photon imaging are shown for three of these neurons. The top three rows in Figure 8C illustrate single-trial fluorescence records, and the bottom row plots the average of multiple trials (dark trace, with individual trials in gray). Likewise, the top row in Figure 8D plots an individual trial, and the bottom shows the average fluorescence response to variable frequencies. Neurons 1 and 2 respond preferentially to one of ten vocalizations (the two-frequency step syllable) but are not tone responsive. Meanwhile, neuron 3 prefers tones, consistent with a border region. Figures S8H and S8I summarizes statistical analysis of call selectivity. These results illustrate the power of multiscale imaging to identify stimulus-specific receptive regions and neurons.

DISCUSSION

Our results demonstrate the enormous utility of multiscale Ca^{2+} imaging of transgenic GCaMP3 mice. By first monitoring activity across all auditory sensory regions to define a global map, followed by scrutiny of individual neurons registered to global coordinates, we readily resolve functional organization within auditory cortex. Indeed, a long-sought key to comprehending the coding of sensory information is just this capability—to monitor populations of neurons whose precise locations within individual brains are known (Averbeck et al., 2006).

Using this strategy in unanesthetized mice, two-photon Ca^{2+} measurements of individual neurons support a strongly organized tonotopic structure in the primary AI auditory cortex of mice, both at the local (<100 μm) and global scales (across AI). These results contrast with those in recent reports that used two-photon Ca^{2+} imaging of neurons (Bandyopadhyay et al., 2010; Chen et al., 2011; Rothschild et al., 2010) but do agree with and enhance the profile of prior microelectrode mapping studies (Guo et al., 2012; Hackett et al., 2011; Stiebler et al., 1997) (Figure S8; Table S1). Though the coarse existence of some cortical tonotopic organization has never been in doubt on the scale of an entire primary auditory field, the divergence from this paradigm at smaller scales in recent two-photon studies has raised the possibility that precise tonotopy may represent an averaging "epiphenomenon" of the electrode method rather than a "valid description of the underlying biology" (Guo et al., 2012). Figure S8 and Table S1 furnish head-to-head comparison among the present and prior studies. Overall, this report may unify newer two-photon imaging and traditional electrode perspectives.

Beyond the issue of tonotopicity, our multiscale approach offers new possibilities: facilitating investigation of other auditory fields, in particular to define sharply contrasting response behaviors in AII; resolving novel organizational features within AII and AAF; and readily identifying and characterizing vocalization-responsive regions and neurons.

Reconciling AI Profiles from Electrode-Based Studies and Two-Photon Ca^{2+} Imaging

The differences in AI tonotopic organization observed by electrode recordings and prior two-photon Ca^{2+} imaging studies could arise from multiple factors. For example, single-unit electrode recordings favor the most active neurons, and multiunit recordings convey population-averaged signals that preferentially weigh the contributions of highly active neurons. By contrast, two-photon Ca^{2+} imaging may encompass a sample that includes numerous weakly active neurons, whose responses could differ from those of their more active counterparts. Another sampling bias could be that two-photon studies tend to focus on superficial layers II/III of cortex that afford better optical resolution, whereas electrode studies commonly target deeper layer IV. Perhaps highly active and tonotopically organized neurons predominate in layer IV, while weakly responding and poorly tuned neurons prevail in superficial layers II/III of cortex. A recent two-photon study argues for such a scenario via explicit comparison of responses in layers IV and II/III (Winkowski and Kanold, 2013). However, the majority of neurons investigated in the present study are from layers II/III (Figure S1Q), which nonetheless exhibit strong tonotopicity (Figures 6A–6C). Moreover, microelectrode studies also confirm significant tonotopic organization in layer II/III (Guo et al., 2012). Still another form of bias relates to the possibility that two-photon Ca^{2+} imaging may incorporate signals of nonneuronal origin, such as from astrocytes (Kerr et al., 2005). The bulk loading of chemical fluorescent dyes used in prior Ca^{2+} imaging studies would robustly label astrocytes (Figures S7A and S7B), yielding a diffuse signal that may be difficult to exclude by simple

(D–F) Single-neuron responses in mid-frequency field of AI, where tone-responsive neurons demonstrate clear tuning to similar middle frequencies. Format as in (A)–(C), but from different mouse, with −40 dB sound attenuation. GCaMP3 under Syn1-Cre. Neurons 1–4 in (E) exhibit mid-frequency tuning. Fields often contained neurons with activity not driven by tones, as illustrated by neuron 5 in (E) (white-circled neuron in [D]). Individual FRAs in (E) scaled to 7.25 events/s, and population FRA in (F) scaled to 1.21 events/s.

(G–I) Neuronal responses in high-frequency field of AI (or UF), where tone-responsive neurons demonstrate tuning to similar high frequencies. Format as in (A)–(C); different mouse than in above panels. Data shown here (but not elsewhere) are from bulk-loaded Fluo-2 chemical-fluorescent dye, illustrating overall similarity to results obtained from GCaMP3. Individual FRAs in (H) scaled to 33.11 events/s, and population FRA in (I) scaled to 4.90 events/s.

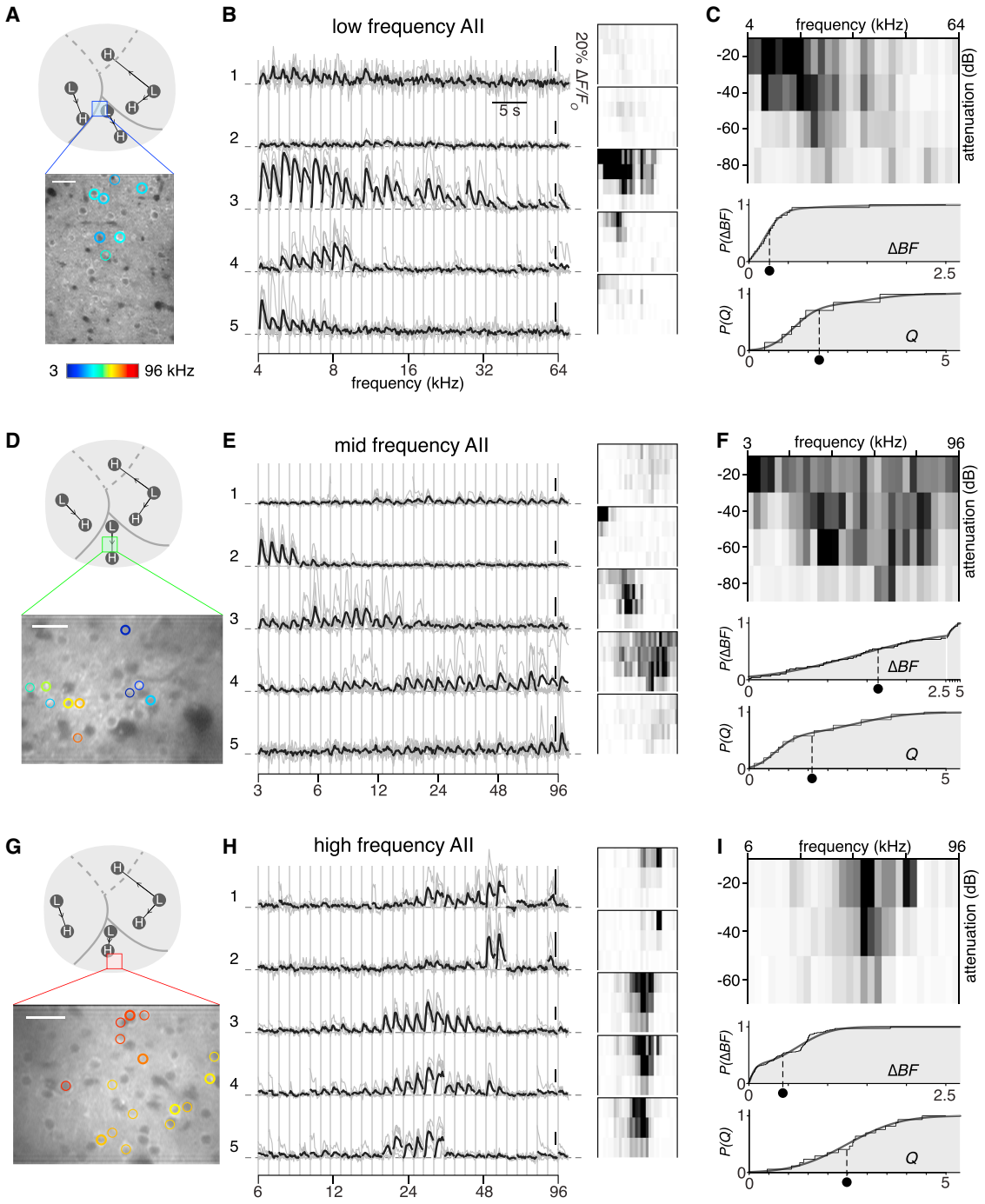

Figure 5. Broad Frequency Tuning and Diverse Best Frequencies in Colocalized AII Neurons

Exemplar low-, middle-, and high-frequency AII fields, format as in Figures 4A–4C.

(A–C) Neuron-by-neuron responses in low-frequency AII field, from mouse expressing GCaMP3 under Syn1-Cre. Neurons exhibit overall preference for low frequencies (B) but with broad frequency responsiveness and diversity of best frequencies. Broad population FRA in (C) supports this trend. Individual and group FRAs scaled to 25 (B) and 2.62 events/s (C).

(B, E, and H) Sound attenuation of −20 dB.

(D–F) Neuron responses in mid-frequency AII field from another mouse expressing GCaMP3 under Syn1-Cre. Broad frequency tuning to divergent best frequencies (E) confirmed by population metrics (F). Note x axis break for Δ*BF* to allow full display of larger Δ*BF*s. Individual and group FRAs scaled to 15.5 (E) and 2.66 events/s (F).

(G–I) Responses in high-frequency AII field from mouse with GCaMP3 under Emx1-Cre. Moderately sharp tuning, albeit with greater Δ*BF* than in corresponding high-frequency areas of AI (cf., Figure 4G–4I). Individual and group FRAs scaled to 17.5 (H) and 6.09 events/s (I).

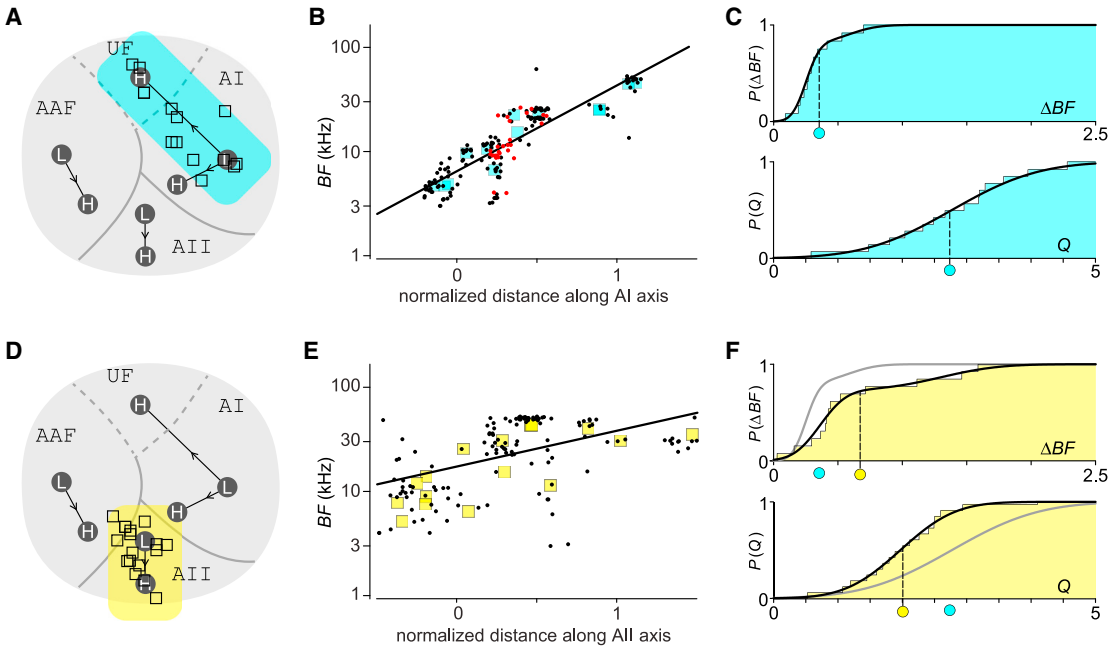

Figure 6. Contrasts in Tonotopic Organization of Mouse AI versus AII Cortex

(A–C) Well-resolved tonotopic gradient via two-photon imaging of individual neurons within AI.

(A) Map of all two-photon imaging fields (squares in translucent ovoid) characterized along ventrodorsal tonotopic axis of AI, as resolved in transcranial maps. Each field registered onto a single canonical map (Figure S6; Supplemental Experimental Procedures).

(B) Best frequencies of neurons versus normalized distance along AI axis, where the "0" coordinate corresponds to the low-frequency pole in AI, and the "1" position marks the high-frequency landmark atop AI (i.e., UF). Each black symbol marks outcome of one neuron, and ensemble of points encompasses all tone-responsive neurons from all fields in (A) (squares). Squares in (B) plot field averages. Good linear correlation (r = 0.88, 154 neurons, $p < 0.001$ via Pearson's analysis) supports strong tonotopy in AI. Normalized distance on AI axis determined by orthogonal projection onto linear axis between low- and high-frequency AI poles, determined in transcranial maps for given neurons. Fields within 300 μm of the axis included. Red symbols, data from single larger field of view, obtained with 25× objective (Figures S8B–S8D).

(C) Summary of cotuning and tuning sharpness for all fields in (A). Top, cumulative distribution of Δ*BF*, as in Figure 4C. Bottom, cumulative distribution of sharpness of tuning (*Q*) averaged across all neurons within individual fields. Black-dashed vertical lines and symbols indicate mean values.

(D–F) Weaker tonotopic gradient in AII, same format as in (A)–(C).

(D) Squares register fields residing near tonotopic axis of AII (translucent ovoid).

(E) *BF* plotted versus normalized position along AII tonotopic axis demonstrates poorer but significant correlation (r = 0.54, 143 neurons, $p < 0.001$ via Pearson's analysis).

(F) Weaker cotuning and tuning sharpness in AII versus AI. Top, cumulative distribution of Δ*BF* for all AII fields in (D) (black with yellow shading). Significant right shift of distribution ($p < 0.042$, two-tailed Mann-Whitney, performed on metrics from 13 AI versus 16 AII fields) compared with AI distribution (fit reproduced in gray for reference) indicates greater diversity of best frequencies at specific AII locales. Bottom, cumulative distribution of *Q* for all AII fields in (D) (black with yellow shading). Significant left shift of distribution ($p < 0.02$, two-tailed Mann-Whitney performed on metrics from 13 AI versus 16 AII fields) compared with AI distribution (fit reproduced in gray for reference) showing decreased sharpness of tuning in AII. Vertical dashed lines and symbols correspond to the mean Δ*BF* and *Q* values for AII (yellow) and AI (cyan).

(B, C, E, and F). Data from mice expressing GCaMP3 under Syn1-Cre (n = 9) and Emx1-Cre (n = 8) and from mice bulk loaded with Fluo-2 (n = 10).

region-of-interest analysis. GCaMP3 sensors, particularly as expressed under the neuron-selective promoter Syn1 used in many of our recordings (Figures S1, S7A, and S7B), are less prone to such crosstalk. A final potential concern is that parvalbumin-expressing GABAergic neurons exhibit broader tuning than excitatory neurons (Li et al., 2014). Thus, selective exclusion of GABAergic neurons (for example, ~2% express GCaMP3 under the Emx1 promoter) (Gorski et al., 2002) may bias results. However, this effect is unlikely to be significant as only ~7% of all auditory cortical neurons express parvalbumin (Yuan et al., 2011).

Beyond sampling bias, two-photon imaging could be especially vulnerable to anesthesia. As auditory cortex is several synapses removed from the cochlea, anesthesia may diminish cortical activity more severely here than in other sensory modalities (Wang, 2007). Electrodes would still detect the resulting sparse spike activity, but fluorescent Ca^{2+} sensors would respond poorly to isolated spikes, making it difficult to resolve response properties (Gaese and Ostwald, 2001; Kindler et al., 1999). The use of unanesthetized mice in the present study may have diminished these challenges (Figure S7E). Finally, the cortical location of neurons sampled by two-photon microscopy may have been uncertain in prior studies. Electrode mapping studies painstakingly sample the spatial extent of auditory cortex, thereby definitively establishing the location of each recording site relative to the overall cortical map. By contrast,

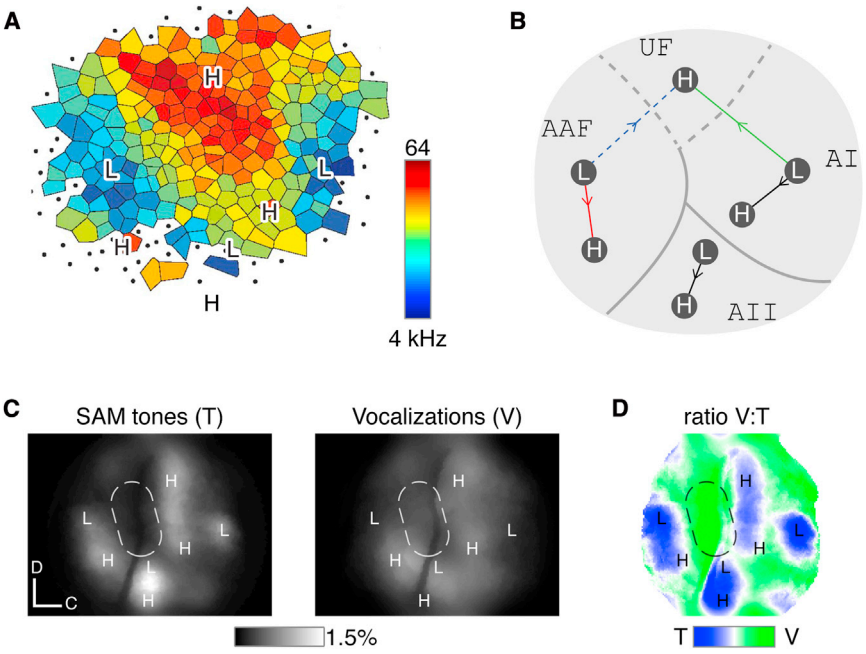

Figure 7. Tone-Insensitive Sector along AI/AII Border

(A) Comparison of low- and high-frequency poles of global transcranial map (from Figure 2B) to electrode-based map (Guo et al., 2012). Landmarks (L and H) translated without scaling or rotation to register low- and high-frequency loci. Ventral landmarks correspond to regions where it is difficult to assign best frequencies using electrodes (dots, indeterminate responsiveness).

(B) Features of primary fields by multiscale imaging. Global map annotated from Figure 2F.

(C) Tone-insensitive region (dashed sector) identified by global transcranial maps from representative experiment. Left subpanel plots fluorescence response averaged across multiple SAM tone frequencies spanning entire mouse receptive range, while right subpanel plots same in response to a set of ten vocalizations (Figure 8A). Dashed oval denotes region insensitive to SAM tones. Both sets of stimuli presented at 20 dB attenuation. GCaMP3 expressed under Syn1-Cre.

(D) Ratio of vocalization to tone responses from same mouse as in (C). Green regions correspond to pixels favoring vocalizations (by 4:1), and blue regions to those favoring SAM tones (by 1:4). Dashed oval same as in (C).

two-photon studies often rely on stereotaxic or anatomic markers to discern the site of Ca^{2+} imaging, yet these markers vary in relation to functional maps within individual animals (Guo et al., 2012; Merzenich et al., 1973), as confirmed by our own global transcranial maps (Figures 2B and 2C). This variability would be especially consequential given the small size of mouse auditory cortex. Beyond suboptimal registration in primary cortex, a field assigned by stereotaxy to AI and AAF may actually reside outside these regions—for example, in AII. This could lead to the appearance of weak tonotopy in primary cortex. The chance of suboptimal registration is reduced in our study by registering fields to specific coordinates in a global map.

Recent electrode studies have begun to engage these issues (Guo et al., 2012; Hackett et al., 2011), but the dissonance between electrode and Ca^{2+} imaging approaches has largely remained. The strong AI tonotopy observed here via two-photon imaging (Figures 6A–6C) thus offers to unify perspectives from Ca^{2+} imaging and decades of electrode studies.

Organization of Auditory Cortical Regions

As described in the results, multiscale imaging allows both confirmation and novel extension of tonotopic organization in primary auditory fields (AI and AAF) (Figures 7A and 7B). Importantly, this strategy also permits exploration of robustly registered secondary areas. New organizational features of AII are thus resolved. Many AII neurons are broadly tuned to an impressive degree (Figure 6F, bottom), as found previously using electrodes (Geissler and Ehret, 2004). Moreover, neighboring AII neurons are disparately tuned (Figure 6F, top)—an insight afforded by two-photon imaging. Finally, AII has a weak but consistent dorsoventral frequency organization (Figure 6E). Altogether, these properties may reflect functions that distinguish AII from the primary fields, such as frequency-invariant, object-based representations.

Concerning more complex stimuli, multiscale imaging permitted rapid localization and interrogation of vocalization-responsive regions and neurons (Figures 7 and 8). This capability is timely, as the encoding of vocalizations in primate auditory cortex has become a potentially tractable realm for studying higher-order processing, where different cortical fields play complementary but as-yet-poorly-understood roles (Romanski and Averbeck, 2009). Vocalization studies in rodents (advantageous for facile transgenic manipulation) would furnish a critical counterpoint; yet, comparatively little is known, with detailed electrode studies mainly focused on AI (Carruthers et al., 2013) and the likely essential role of other subregions sparingly explored (Geissler and Ehret, 2004). In this regard, our multiscale imaging approach could prove particularly advantageous. First, global maps for each mouse allow precise registration of two-photon fields responsive to vocalization, a feature especially critical if multiple cortical subregions collaborate in sound processing. Second, responses to vocalizations can be recorded transcranially, allowing the experimenter to rapidly focus on particularly informative loci. In primates, vocalizations may even involve aspects of prefrontal cortex, in addition to the auditory fields per se (Romanski and Averbeck, 2009). Our global transcranial imaging could facilitate a search for similarly expansive involvement of cortex in mice. An exciting frontier lies ahead.

More broadly, the new information from mice may comment on auditory cortical organization across other species. In rat, similarly arranged primary fields AAF and AI are observed (Polley et al., 2007; Wu et al., 2006). Interestingly, the coarse analog of the mouse AII region would be the rat VAF secondary field, which also demonstrates a weaker tonotopic organization than AI while

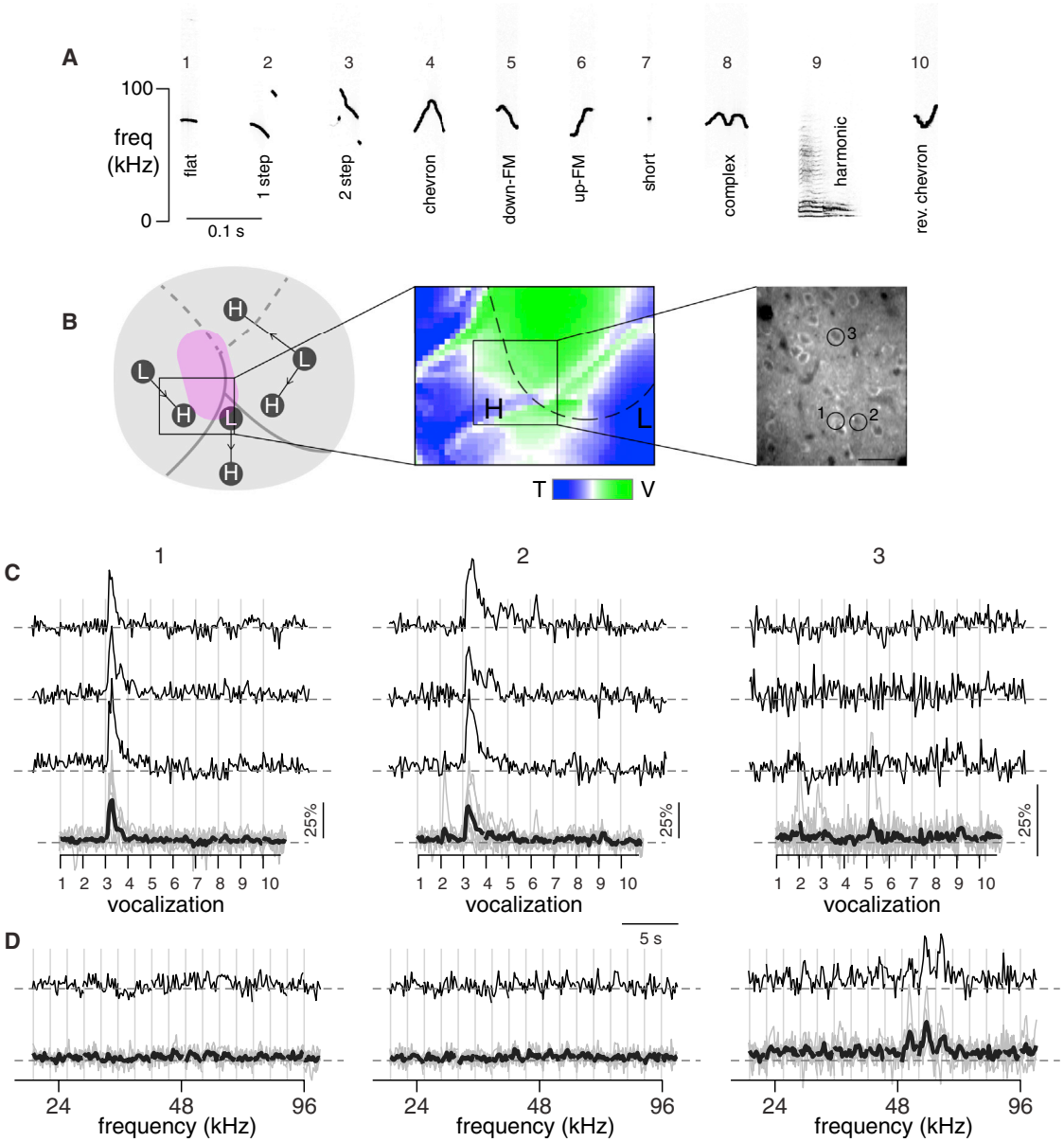

Figure 8. Vocalization-Selective Neurons Identified by Multiscale Ca^{2+} Imaging

(A) Spectrograms of ten adult vocalizations adapted from online database (Grimsley et al., 2011). Silent periods removed for clarity.

(B) Global map for this mouse identifies tone-insensitive region highlighted by magenta oval (left subpanel). High-frequency AAF region (rectangle) overlaid on color map showing ratio of vocalization to tone responses (middle subpanel). Right subpanel displays corresponding two-photon field (scale bar, 30 μm). GCaMP3 under Syn1-Cre (another mouse than in Figure 7).

(C) Single-neuron responses to vocalizations. Single trials (top three rows) illustrate responses for three neurons identified in (B). Bottom row plots average of multiple trials (dark trace, with individual trials in gray).

(D) Single-neuron response to SAM tones. Format as in (C) except only one trial is shown. No neurons in this field responded below 24 kHz, so traces are truncated.

nonetheless exhibiting a ventrally directed low-to-high-frequency gradient (Polley et al., 2007). Another potential commonality relates to reports in rat of a tone-insensitive region along the border of AAF and AI, similar to our murine findings (Figure 7C, ovoid) (Polley et al., 2007; Wu et al., 2006). It would then be interesting if this region of rat would also support representation of more complex stimuli. As with mice, cats also exhibit a coarsely similar arrangement of primary AAF and AI fields, with a ventrally situated secondary AII field (Winer and Lee, 2007). It is intriguing that a multimodal AES locus resides near the junction of these three fields. Likewise, in marmosets, a pitch center resides at the juncture between primary R and AI fields (Bendor and Wang, 2005).

Perhaps, there is a coarsely preserved organizational feature for representing more complex stimuli at this locus.

General Applicability of the Multiscale Approach

The ability of two-photon Ca^{2+} imaging to monitor activity across hundreds of neighboring neurons is powerful. Yet, cortical organization extends beyond neuronal activity within local fields to interacting sensory cortices that encompass larger spatial dimensions (Knöpfel, 2012; Wang, 2007). Accordingly, connecting the activity of individual neurons to more global events and coordinates is crucial. For instance, for investigating cortical rearrangement during development or altered experience (Buonomano and Merzenich, 1998; de Villers-Sidani et al., 2008; Guo et al., 2012; Karmarkar and Dan, 2006), multiscale Ca^{2+} imaging approach could significantly expand the scope and resolution of experiments, thus far limited to electrode methods. Additionally, transcranial global imaging could simultaneously survey and register multiple cortical fields that collectively orchestrate higher-order functions (Eliades and Wang, 2008; Hubbard and Ramachandran, 2005). Indeed, several two-photon studies have already employed intrinsic imaging strategies to correspond high-resolution neuronal data to the overall layout of cortex (Andermann et al., 2011; Marshel et al., 2011; Olcese et al., 2013). Other intrinsic imaging studies have also illumined the large-scale organization of rodent auditory cortex (Bathellier et al., 2012; Kalatsky et al., 2005; Moczulska et al., 2013; Polley et al., 2007). However, such intrinsic imaging necessitates considerable multitrial averaging, thus limiting convenience and breadth of experiments. By contrast, the multiscale imaging of GCaMP3 transgenic mice described here furnishes global maps within single trials, facilitating views of rapidly evolving plasticity and time-varying adaptation to specific stimuli (Taaseh et al., 2011) and expanding the dimensionality of stimuli and experimental complexity that can be accommodated. In the future, our imaging approaches are potentially miniaturizable, permitting readouts in awake behaving animals. As transgenic models with improved sensors arise (Chen et al., 2013), multiscale imaging should prove increasingly useful for probing the function of brain circuitry at large and small scales.

EXPERIMENTAL PROCEDURES

Animal Surgery and General Procedures

All animal procedures approved by Johns Hopkins Institutional Animal Care and Use Committee. Floxed GCaMP3 mice (R26-lsl-GCaMP3, Ai38 from Jackson Labs; JAX catalog number 014538) (Zariwala et al., 2012) were crossed with Syn1-Cre mice (JAX catalog number 003966) (Zhu et al., 2001) or Emx1-Cre mice (JAX catalog number 005628) (Gorski et al., 2002), resulting in GCaMP3-Syn1 or GCaMP3-Emx1 mice used for experiments. Anesthesia, surgery, and imaging methods detailed in Supplemental Experimental Procedures. All imaging performed on unanesthetized mice.

Ca^{2+} Dye Injection and Cranial Window Preparation

In a minority of mice (e.g., Figures 4G–4I), bulk-loaded Fluo-2 (TEFLabs) was used for Ca^{2+} imaging. For Ca^{2+} imaging of neurons (GCaMP3 or Fluo-2), a glass coverslip was often affixed atop craniotomy to dampen pulsations.

Widefield Transcranial Imaging of GCaMP3

We typically performed widefield imaging through a thinned skull, using 460 nm excitation focused 0–200 μm beneath dura through a 10× 0.25 NA objective (Olympus). The 540 nm emission collected onto a CCD camera at 20 Hz.

Two-Photon Ca^{2+} Imaging

Imaging was performed with an Ultima system (Prairie Technologies). Excitation at 950 nm from a mode-locked laser was raster scanned at 5–12 Hz with emission collected in red (607/45 nm) and green (525/70 nm) channels. A 40× 0.8 NA objective (Olympus) used. As noted, 25× objective (Olympus XLPlan N) was used in some instances to afford a larger field of view.

Auditory Stimulation

Microscope located in sound-attenuated room (Acoustical Solutions, AudioSeal ABSC-25) with noisy equipment placed outside. Sounds delivered by free-field speaker (Tucker-Davis Technologies, ES1) 12 cm from right ear. Ambient background noise significantly weaker than the softest stimuli presented (Figures S4G and S4H).

Immunohistochemistry

Mice were anesthetized with pentobarbital and perfused with freshly prepared 4% paraformaldehyde (PFA). Brains were postfixed in 4% PFA overnight at 4°C and stored in phosphate buffered saline (PBS) at 4°C until processed. Thirty-five-micrometer-thick coronal brain sections cut with vibratome were incubated overnight with primary antibodies against GFAP and NeuN. After rinsing, sections further incubated with secondary antibodies, rinsed, and mounted on superfrost glass slides. Confocal imaging was then performed.

Data Analysis

Transcranial Ca^{2+} images were processed by a structured sparse encoding algorithm (Haeffele et al., 2014). For two-photon Ca^{2+} imaging of neurons, fluorescence signals were directly used to calculate output-versus-frequency response profiles (e.g., Figure 3C). A deconvolution method was subsequently applied to estimate spike probabilities (Vogelstein et al., 2010), used for analyzing FRAs as well as *BF* and *Q* metrics described below. For registration, transcranial maps and vascular fiduciaries were used to localize individual neurons. To compare across mice, elastic registration of each animal's coordinates to a canonical coordinate system was performed. *BF* was the frequency evoking strongest responses at threshold. Bandwidth was calculated as the average of the half-maximal width of Gaussian fits to output-versus-frequency plots and the frequency range eliciting greater than half maximum responses. Δ*BF* was defined as the absolute difference in *BF* for each pair of tone-responsive neurons in a field, measured in octaves. *Q* factor was the *BF* at threshold divided by maximum bandwidth at any sound level.

Extended Methods

More complete methods appear in the Supplemental Experimental Procedures.

SUPPLEMENTAL INFORMATION

Supplemental Information includes eight figures, one table, and Supplemental Experimental Procedures and can be found with this article online at http://dx.doi.org/10.1016/j.neuron.2014.07.009.

ACKNOWLEDGMENTS

We wish to thank M. Ben-Johny and A. Djamanakova for assistance on the manuscript, X. Wang for discussions, P.J. Adams for mouse care, X. Song for loaning 25× objective, and P. Worley for the Syn1-Cre mouse line. This work was supported by grants from the Kleberg Foundation (to D.T.Y.), NINDS (to D.T.Y.), NIH (MSTP fellowship to J.B.I.), and NIDCD (NRSA fellowship to B.D.H.).

Accepted: July 3, 2014
Published: July 31, 2014

REFERENCES

Andermann, M.L., Kerlin, A.M., Roumis, D.K., Glickfeld, L.L., and Reid, R.C. (2011). Functional specialization of mouse higher visual cortical areas. Neuron *72*, 1025–1039.

Averbeck, B.B., Latham, P.E., and Pouget, A. (2006). Neural correlations, population coding and computation. Nat. Rev. Neurosci. *7*, 358–366.

Bandyopadhyay, S., Shamma, S.A., and Kanold, P.O. (2010). Dichotomy of functional organization in the mouse auditory cortex. Nat. Neurosci. *13*, 361–368.

Bathellier, B., Ushakova, L., and Rumpel, S. (2012). Discrete neocortical dynamics predict behavioral categorization of sounds. Neuron *76*, 435–449.

Bendor, D., and Wang, X. (2005). The neuronal representation of pitch in primate auditory cortex. Nature *436*, 1161–1165.

Buonomano, D.V., and Merzenich, M.M. (1998). Cortical plasticity: from synapses to maps. Annu. Rev. Neurosci. *21*, 149–186.

Carruthers, I.M., Natan, R.G., and Geffen, M.N. (2013). Encoding of ultrasonic vocalizations in the auditory cortex. J. Neurophysiol. *109*, 1912–1927.

Chen, X., Leischner, U., Rochefort, N.L., Nelken, I., and Konnerth, A. (2011). Functional mapping of single spines in cortical neurons in vivo. Nature *475*, 501–505.

Chen, T.W., Wardill, T.J., Sun, Y., Pulver, S.R., Renninger, S.L., Baohan, A., Schreiter, E.R., Kerr, R.A., Orger, M.B., Jayaraman, V., et al. (2013). Ultrasensitive fluorescent proteins for imaging neuronal activity. Nature *499*, 295–300.

de Villers-Sidani, E., and Merzenich, M.M. (2011). Lifelong plasticity in the rat auditory cortex: basic mechanisms and role of sensory experience. Prog. Brain Res. *191*, 119–131.

de Villers-Sidani, E., Simpson, K.L., Lu, Y.F., Lin, R.C., and Merzenich, M.M. (2008). Manipulating critical period closure across different sectors of the primary auditory cortex. Nat. Neurosci. *11*, 957–965.

Eliades, S.J., and Wang, X. (2008). Neural substrates of vocalization feedback monitoring in primate auditory cortex. Nature *453*, 1102–1106.

Gaese, B.H., and Ostwald, J. (2001). Anesthesia changes frequency tuning of neurons in the rat primary auditory cortex. J. Neurophysiol. *86*, 1062–1066.

Geissler, D.B., and Ehret, G. (2004). Auditory perception vs. recognition: representation of complex communication sounds in the mouse auditory cortical fields. Eur. J. Neurosci. *19*, 1027–1040.

Gorski, J.A., Talley, T., Qiu, M., Puelles, L., Rubenstein, J.L., and Jones, K.R. (2002). Cortical excitatory neurons and glia, but not GABAergic neurons, are produced in the Emx1-expressing lineage. J. Neurosci. *22*, 6309–6314.

Grimsley, J.M., Monaghan, J.J., and Wenstrup, J.J. (2011). Development of social vocalizations in mice. PLoS ONE *6*, e17460.

Grinvald, A., and Hildesheim, R. (2004). VSDI: a new era in functional imaging of cortical dynamics. Nat. Rev. Neurosci. *5*, 874–885.

Guo, W., Chambers, A.R., Darrow, K.N., Hancock, K.E., Shinn-Cunningham, B.G., and Polley, D.B. (2012). Robustness of cortical topography across fields, laminae, anesthetic states, and neurophysiological signal types. J. Neurosci. *32*, 9159–9172.

Hackett, T.A., Barkat, T.R., O'Brien, B.M., Hensch, T.K., and Polley, D.B. (2011). Linking topography to tonotopy in the mouse auditory thalamocortical circuit. J. Neurosci. *31*, 2983–2995.

Haeffele, B.D., Young, E.D., and Vidal, R. (2014). Structured Low-Rank Matrix Factorization: Optimality, Algorithm, and Applications to Image Processing. In Proceedings of The 31st International Conference on Machine Learning (Beijing, China).

Honma, Y., Tsukano, H., Horie, M., Ohshima, S., Tohmi, M., Kubota, Y., Takahashi, K., Hishida, R., Takahashi, S., and Shibuki, K. (2013). Auditory cortical areas activated by slow frequency-modulated sounds in mice. PLoS ONE *8*, e68113.

Hubbard, E.M., and Ramachandran, V.S. (2005). Neurocognitive mechanisms of synesthesia. Neuron *48*, 509–520.

Joachimsthaler, B., Uhlmann, M., Miller, F., Ehret, G., and Kurt, S. (2014). Quantitative analysis of neuronal response properties in primary and higher-order auditory cortical fields of awake house mice (Mus musculus). Eur. J. Neurosci. *39*, 904–918.

Kaas, J.H. (1997). Topographic maps are fundamental to sensory processing. Brain Res. Bull. *44*, 107–112.

Kaas, J.H. (2011). The evolution of auditory cortex: the core areas. In The Auditory Cortex, J.A. Winer and C.E. Schreiner, eds. (USA: Springer), pp. 407–427.

Kalatsky, V.A., Polley, D.B., Merzenich, M.M., Schreiner, C.E., and Stryker, M.P. (2005). Fine functional organization of auditory cortex revealed by Fourier optical imaging. Proc. Natl. Acad. Sci. USA *102*, 13325–13330.

Karmarkar, U.R., and Dan, Y. (2006). Experience-dependent plasticity in adult visual cortex. Neuron *52*, 577–585.

Kerr, J.N., Greenberg, D., and Helmchen, F. (2005). Imaging input and output of neocortical networks in vivo. Proc. Natl. Acad. Sci. USA *102*, 14063–14068.

Kindler, C.H., Eilers, H., Donohoe, P., Ozer, S., and Bickler, P.E. (1999). Volatile anesthetics increase intracellular calcium in cerebrocortical and hippocampal neurons. Anesthesiology *90*, 1137–1145.

Knöpfel, T. (2012). Genetically encoded optical indicators for the analysis of neuronal circuits. Nat. Rev. Neurosci. *13*, 687–700.

Li, L.Y., Xiong, X.R., Ibrahim, L.A., Yuan, W., Tao, H.W., and Zhang, L.I. (2014). Differential Receptive Field Properties of Parvalbumin and Somatostatin Inhibitory Neurons in Mouse Auditory Cortex. Cereb. Cortex. http://dx.doi.org/10.1093/cercor/bht417.

Marshel, J.H., Garrett, M.E., Nauhaus, I., and Callaway, E.M. (2011). Functional specialization of seven mouse visual cortical areas. Neuron *72*, 1040–1054.

Merzenich, M.M., Knight, P.L., and Roth, G.L. (1973). Cochleotopic organization of primary auditory cortex in the cat. Brain Res. *63*, 343–346.

Mikaelian, D.O., Warfield, D., and Norris, O. (1974). Genetic progressive hearing loss in the C57-b16 mouse. Relation of behavioral responses to chochlear anatomy. Acta Otolaryngol. *77*, 327–334.

Moczulska, K.E., Tinter-Thiede, J., Peter, M., Ushakova, L., Wernle, T., Bathellier, B., and Rumpel, S. (2013). Dynamics of dendritic spines in the mouse auditory cortex during memory formation and memory recall. Proc. Natl. Acad. Sci. USA *110*, 18315–18320.

Ohki, K., Chung, S., Ch'ng, Y.H., Kara, P., and Reid, R.C. (2005). Functional imaging with cellular resolution reveals precise micro-architecture in visual cortex. Nature *433*, 597–603.

Olcese, U., Iurilli, G., and Medini, P. (2013). Cellular and synaptic architecture of multisensory integration in the mouse neocortex. Neuron *79*, 579–593.

Pickles, J.O. (2012). An introduction to the physiology of hearing. (United Kingdom: Emerald Group Publishing Limited).

Polley, D.B., Read, H.L., Storace, D.A., and Merzenich, M.M. (2007). Multiparametric auditory receptive field organization across five cortical fields in the albino rat. J. Neurophysiol. *97*, 3621–3638.

Romanski, L.M., and Averbeck, B.B. (2009). The primate cortical auditory system and neural representation of conspecific vocalizations. Annu. Rev. Neurosci. *32*, 315–346.

Rothschild, G., Nelken, I., and Mizrahi, A. (2010). Functional organization and population dynamics in the mouse primary auditory cortex. Nat. Neurosci. *13*, 353–360.

Stiebler, I., Neulist, R., Fichtel, I., and Ehret, G. (1997). The auditory cortex of the house mouse: left-right differences, tonotopic organization and quantitative analysis of frequency representation. J. Comp. Physiol. A Neuroethol. Sens. Neural Behav. Physiol. *181*, 559–571.

Svoboda, K., and Yasuda, R. (2006). Principles of two-photon excitation microscopy and its applications to neuroscience. Neuron *50*, 823–839.

Taaseh, N., Yaron, A., and Nelken, I. (2011). Stimulus-specific adaptation and deviance detection in the rat auditory cortex. PLoS ONE *6*, e23369.

Taberner, A.M., and Liberman, M.C. (2005). Response properties of single auditory nerve fibers in the mouse. J. Neurophysiol. *93*, 557–569.

Takahashi, K., Hishida, R., Kubota, Y., Kudoh, M., Takahashi, S., and Shibuki, K. (2006). Transcranial fluorescence imaging of auditory cortical plasticity regulated by acoustic environments in mice. Eur. J. Neurosci. *23*, 1365–1376.

Tian, L., Hires, S.A., Mao, T., Huber, D., Chiappe, M.E., Chalasani, S.H., Petreanu, L., Akerboom, J., McKinney, S.A., Schreiter, E.R., et al. (2009). Imaging neural activity in worms, flies and mice with improved GCaMP calcium indicators. Nat. Methods *6*, 875–881.

Vogelstein, J.T., Packer, A.M., Machado, T.A., Sippy, T., Babadi, B., Yuste, R., and Paninski, L. (2010). Fast nonnegative deconvolution for spike train inference from population calcium imaging. J. Neurophysiol. *104*, 3691–3704.

Wang, X. (2007). Neural coding strategies in auditory cortex. Hear. Res. *229*, 81–93.

Winer, J.A., and Lee, C.C. (2007). The distributed auditory cortex. Hear. Res. *229*, 3–13.

Winkowski, D.E., and Kanold, P.O. (2013). Laminar transformation of frequency organization in auditory cortex. J. Neurosci. *33*, 1498–1508.

Wu, G.K., Li, P., Tao, H.W., and Zhang, L.I. (2006). Nonmonotonic synaptic excitation and imbalanced inhibition underlying cortical intensity tuning. Neuron *52*, 705–715.

Yuan, K., Fink, K.L., Winer, J.A., and Schreiner, C.E. (2011). Local connection patterns of parvalbumin-positive inhibitory interneurons in rat primary auditory cortex. Hear. Res. *274*, 121–128.

Zariwala, H.A., Borghuis, B.G., Hoogland, T.M., Madisen, L., Tian, L., De Zeeuw, C.I., Zeng, H., Looger, L.L., Svoboda, K., and Chen, T.W. (2012). A Cre-dependent GCaMP3 reporter mouse for neuronal imaging in vivo. J. Neurosci. *32*, 3131–3141.

Zhu, Y., Romero, M.I., Ghosh, P., Ye, Z., Charnay, P., Rushing, E.J., Marth, J.D., and Parada, L.F. (2001). Ablation of NF1 function in neurons induces abnormal development of cerebral cortex and reactive gliosis in the brain. Genes Dev. *15*, 859–876.

Neuron, Volume *83*

Supplemental Information

Multiscale Optical Ca^{2+} Imaging of Tonal Organization in Mouse Auditory Cortex

John B. Issa, Benjamin D. Haeffele, Amit Agarwal, Dwight E. Bergles, Eric D. Young, and David T. Yue

Supplemental Information

Supplemental Figures

1. **Immunohistochemistry of transgenic mice, related to Figure 6**
2. **Unsorted transcranial responses to tones and deblurring of images, related to Figure 1**
3. **Stability of landmarks against duration and sound level, related to Figure 2**
4. **Further details on formation of transcranial map, related to Figure 2**
5. **Registration of imaging fields, related to Figures 2, 6, and 7**
6. **Detailed work-up of single neuron tuning under two-photon imaging, related to Figure 3**
7. **Ca^{2+} transients under different conditions, related to Figures 1-6**
8. **Co-tuning and tonotopy among neighboring neurons in present study versus prior work, related to Figures 6 and 8**

Supplemental Tables

1. **Comparing co-tuning among neighboring neurons and adherence to a tonotopic axis in present study versus that reported in Bandyopadhyay *et al* (2010) *Nature Neuroscience,* and Rothschild *et al* (2010) *Nature Neuroscience,* related to Figure 6**

Online Extended Experimental Procedures

Supplemental References

Figure S1

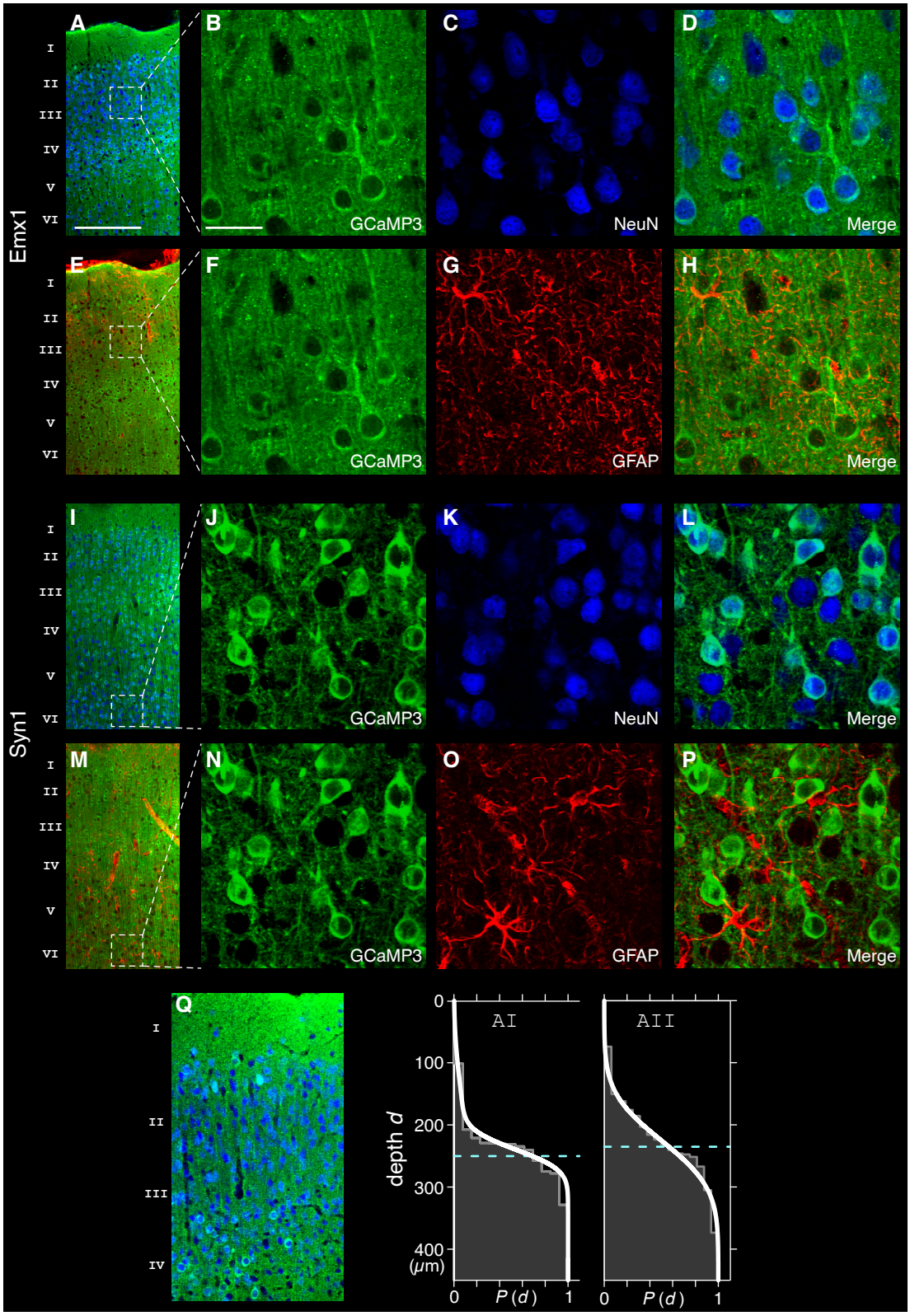
Emx1
Syn1
A
B
C
D
E
F
G
H
I
J
K
L
M
N
O
P
Q
I
II
III
IV
V
VI
GCaMP3
NeuN
Merge
GFAP
AI
AII
depth d
(μm)
P(d)
0
100
200
300
400
1

Figure S1. Immunohistochemistry of transgenic mice, related to Figure 6

(A-H) Immunostained slices from a male P80 GCaMP3-Emx1 mouse. After perfusion with 4% PFA, 50 μm coronal slices were taken ~2 mm caudal to bregma. Imaged sections were centered on presumptive auditory cortex, ~4 mm lateral to midline. NeuN was labeled at 546 nm and shown in blue, GCaMP3 at 488 and shown in green, and GFAP at 647 and shown in red.

(A) Low magnification view of GCaMP3 and NeuN staining. Labels on the left indicate assumed locations of cortical layers. White square registers area imaged under higher magnification and shown in B-D. GCaMP3 is expressed diffusely throughout all cortical layers (scale bar, 250 μm).

(B-D) High magnification view of GCaMP3 and NeuN. These cells are likely in layers II/III. GCaMP3 signal is diffuse with a few neurons showing enhanced expression that corresponds to locations of neuronal cell bodies as indicated by the NeuN signal (scale bar, 30 μm).

(E) Low magnification view of GCaMP3 and GFAP signal. GFAP (red) is a marker of astrocytes. This field is identical to A.

(F-H) High magnification view of GCaMP3 and GFAP. This field is identical to B-D. Note that F is reproduced from B. In the merged image, there is minimal overlap of GCaMP3 and GFAP signal, indicating that the majority of GCaMP3-Emx1 expression is in neurons.

(I-P) Immunostained slices from a female P68 GCaMP3-Syn1 mouse. These are displayed using a format identical to A-H. This time, area of high magnification (highlighted by white box in I and M) is taken in a deeper cortical layer, likely corresponding to layer VI. In comparison to GCaMP3-Emx1 staining shown in A-H, the GCaMP3-Syn1 expression is more sharply localized to neuronal cell bodies as indicated by higher contrast between neuronal cell bodies and the neuropil background signal (compare B with J). Again, there is minimal overlap of GCaMP3 and GFAP signal (P). Finally, note that there is incomplete expression under both promoters as not all NeuN-stained neurons are expressing GCaMP3 (D and L). The lower proportion of expressing neurons in Emx1 mice may partially reflect exclusion of Emx1 from interneurons.

(Q) Depth profile of two-photon fields. Shown on the left panel is a low-magnification image of a slice from the same GCaMP3-Emx1 mouse shown in A-H. Presumptive layer locations are

labeled. On the right are cumulative histograms of the depths of the two-photon fields shown in Figure 6. There are 13 fields from AI and 16 fields from AII. Horizontal dashed lines indicate mean depths. The majority of fields are located at 200-300 μm deep, likely corresponding to layers II/III of cortex.

Figure S2

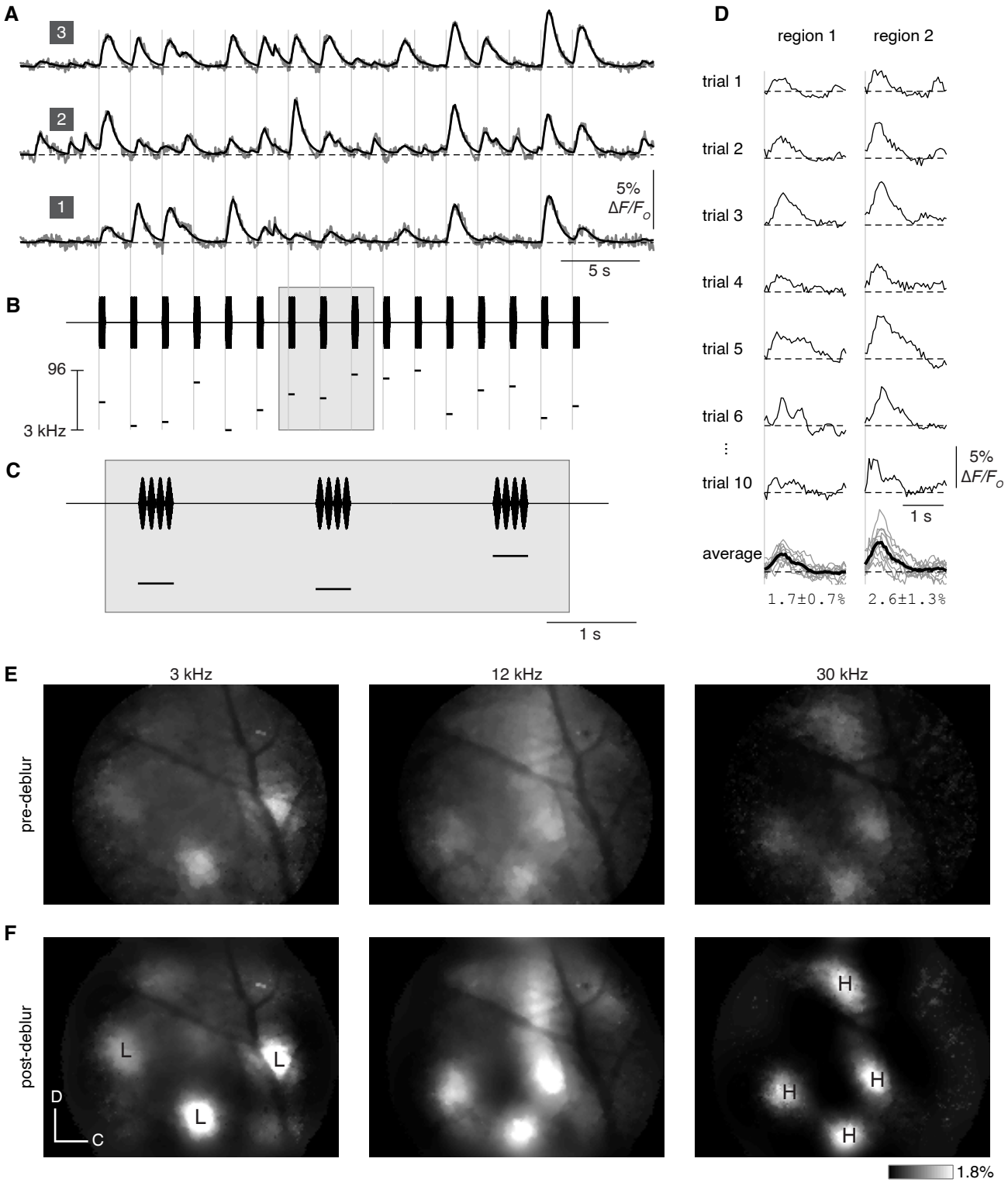
A
3
2
1
5%
ΔF/F_o
5 s
B
96
3 kHz
C
1 s
D
region 1
region 2
trial 1
trial 2
trial 3
trial 4
trial 5
trial 6
trial 10
average
5%
ΔF/F_o
1 s
1.7±0.7%
2.6±1.3%
E
3 kHz
12 kHz
30 kHz
pre-deblur
F
post-deblur
L
L
L
D
C
H
H
H
H
1.8%

Figure S2. Unsorted transcranial responses to tones and deblurring of images, related to Figure 1

(A) Ca^{2+} activity induced by random-ordered SAM tones from the three regions marked in Figure 1B. Shown are single-trial fluorescence responses. The original baseline-corrected signal is shown in gray, and the sparse-encoding processed waveform in black (see Experimental Procedures). These are the same traces shown in Figure 1C but unsorted.

(B) Auditory stimulus for the responses in panel A. Upper panel shows the pressure waveform and lower panel shows the spectrogram, highlighting the randomized tone order.

(C) Blow-up of shaded region from B. SAM tones (10 Hz modulation, 400 ms duration) were used.

(D) Responses to ten repeats of the same stimulus, a 60 kHz SAM tone presented at 20 dB attenuation. Top seven rows show individual trials. Bottom row shows individual trials plotted in gray and averaged responses from multiple trials in black with mean and standard deviation over the first second of each response shown below the traces. Each column corresponds to a different 180×180 μm^2 region. Data collected from a different experiment than other panels of the figure.

(E) Responses at 3 different frequencies before applying image deblur. These are baseline-corrected averages taken over the first 400 msec after each stimulus. As described in Experimental Procedures (Transcranial Image Analysis), image normalization and the structured sparse encoding algorithm have been applied; the product *AZ* is being shown.

(F) Responses after deblurring with a 2-D Gaussian window ($\sigma = 200$ μm) using the Lucy-Richardson deconvolution method to reduce susceptibility to noise. Dorsal-caudal spatial scale bar on lower left denotes 300 μm along each dimension.

Figure S3

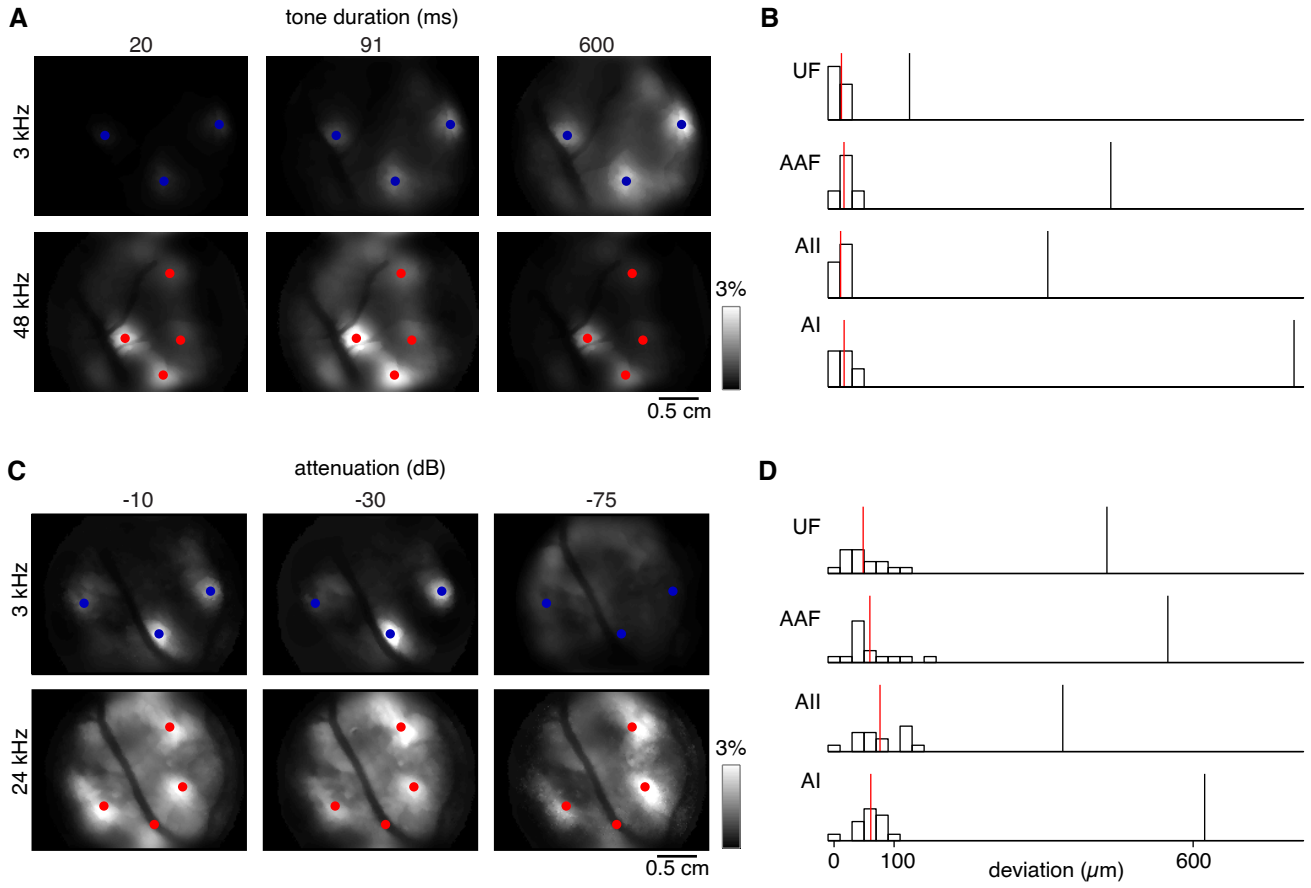
A
tone duration (ms)
20
91
600
3 kHz
48 kHz
3%
0.5 cm
B
UF
AAF
AII
AI
C
attenuation (dB)
-10
-30
-75
3 kHz
24 kHz
3%
0.5 cm
D
UF
AAF
AII
AI
0
100
600
deviation (μm)

Figure S3. Stability of landmarks against duration and sound level, related to Figure 2

(A) Responses at 3 different tone durations and at 2 different frequencies. Pure tones were used. Blue and red dots mark the weighted mean of activity peaks at the shortest duration tested for 3 and 48 kHz, respectively. In total, 6 frequencies (3 to 96 kHz) and 10 durations (20 to 600 ms, logarithmically spaced) were tested.

(B) Histogram of deviations in peak centers at different durations. Peak centers were found for each tone frequency and duration pair. Low frequency sounds typically elicited 3 peaks and high frequency sounds elicited 4 peaks, as seen in A. Based on these peaks, the imaged field was divided into four regions (AI, AAF, UF, and AII). For each region, distances between peak centers for different tone durations of the same frequency were calculated. This was done for all pairwise combinations of durations, at each frequency, if that frequency-duration pair elicited a significant response. A histogram of these distances is shown for each region as open black rectangles (normalized to sum to 1; 20 μm bin widths). The mean value of these distances is marked by the vertical red line. Finally, for comparison, the largest distance between peak centers at any frequency and duration within a region was found and is plotted as the vertical black line. Height of lines is 75%. As can be appreciated, changing tone duration produces little variability in the location of the response for a given tone frequency.

(C) Responses at 3 different attenuation levels and at 2 different frequencies. Display format is same as in A. We tested a total of 16 frequencies (3 to 96 kHz) and 15 attenuation levels (-10 to -80 dB in 5 dB steps). SAM tones (10 Hz modulation, 400 ms duration) were used. Data is a subset of what is shown in Figure 2A. Note lack of response to 3 kHz tone at -75 dB.

(D) Histogram of deviations in peak centers at different attenuation levels. Format is same as in B. Deviations with respect to attenuation level (D) are larger than with respect to tone duration (B); however, they are typically <100 μm and are much less than the span of each respective region (vertical black line).

Figure S4

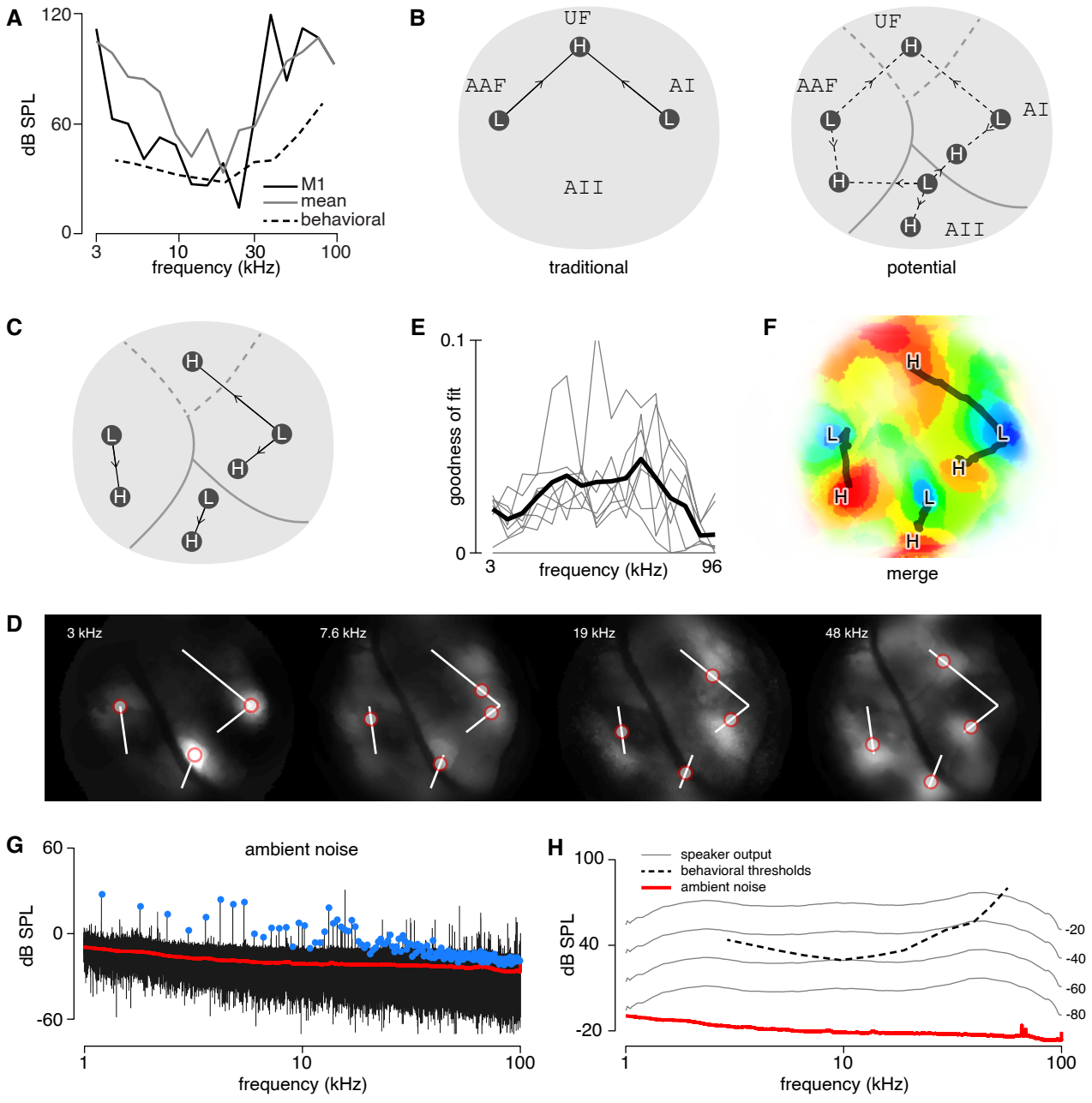
A
120
60
0
dB SPL
3
10
30
100
frequency (kHz)
M1
mean
behavioral
B
UF
AAF
AI
AII
traditional
potential
C
D
3 kHz
7.6 kHz
19 kHz
48 kHz
E
0.1
0
goodness of fit
3
frequency (kHz)
96
F
merge
G
ambient noise
60
0
-60
dB SPL
1
10
100
frequency (kHz)
H
speaker output
behavioral thresholds
ambient noise
100
40
-20
dB SPL
-20
-40
-60
-80
1
10
100
frequency (kHz)

Figure S4. Further details on formation of transcranial map, related to Figure 2

(A) Absolute thresholds estimated from whole-field transcranial FRAs. For the experiment shown in Figures 2A-2B, we estimated the hearing thresholds as detailed in Experimental Procedures (Response Metrics). This estimate is labeled as M1 (solid black curve); it is taken from the same experiment shown in Figure 2B. We then estimated and averaged thresholds across all 7 mice used for the canonical merge shown in Figure 2E. This estimate ("mean") is the solid gray curve. Finally, we superimposed published behavioral thresholds obtained from C57BL/6 mice taken at 2.28 months of age (dashed black curve). Below 30 kHz, thresholds are in good agreement, with some disagreement at higher frequencies.

(B) Tonotopic gradients observed via transcranial Ca^{2+} imaging. Prior studies observed two tonotopic gradients as depicted in the left subpanel, one in AI and another in AAF. These gradients are computed as the path of steepest change in preferred frequency. However, for robust fiducial orientation in our imaging configuration, we favored calculation of tonotopic gradients based on local maxima of response strength with increasing frequency of tone presentations. Given the observations of 3 low-frequency and 4 high-frequency loci, more than two tonotopic gradients could in principle exist. Some of these possible gradient configurations are depicted as dotted lines in the right subpanel.

(C) Best-fitting tonotopic gradient configuration of 243 possible arrangements of low-to-high frequency gradients (where each arrangement was comprised of four gradients). This arrangement corresponds to that used in the main text (e.g., Figure 2F).

(D) Determining path of best-fitting tonotopic gradient. At each frequency sampled, we positioned a Gaussian function with $\sigma = 250$ μm (denoted by red circle) along each low-to-high-frequency trajectory, so as to best fit local signal intensities. This fit was achieved by maximizing a goodness-of-fit parameter defined as the dot product between the bump and the actual fluorescence signals. The resulting bump locations at various frequencies is shown in the subpanels (left to right corresponds to increasing frequencies as labeled).

(E) Goodness of fit plotted against 16 frequencies tested (3 to 96 kHz) for configuration in panel C. The thin gray lines display the outcome from seven individual experiments, and the thick black line shows the average result. The area under curves was taken as the overall goodness of fit. A similar analysis was performed on all 243 potential gradient sets, and the configuration shown in panel C scored best for all seven experiments.

(F) Detailed tracking (dark gray lines) of maximally responding loci across incrementally increasing frequencies, based on a superset of results like those shown in panel D optimized to each local center-of-mass. The map here (reproduced from main text Figure 2E) corresponds to the merged layout aggregated from seven individual experiments.

(G) Power spectrum of background ambient noise with galvanometer engaged (black), at mouse right ear. The larger peaks are mostly harmonics of the fundamental galvanometer frequency ~600 Hz (blue symbols). Red trace shows smoothed spectrum for purposes of subsequent comparison. Spectrum levels shown in 0.1-Hz bands.

(H) Comparison of speaker sound levels at various attenuation levels (gray curves, smoothed) to background ambient noise (red trace, copied from Figure SG). Dashed curve shows behavioral response thresholds from Figure S4A. Overall, for frequencies used in experiments (3 to 96 kHz), background noise is > 20 dB weaker than the softest sound levels used (-80 dB attenuation).

Figure S5

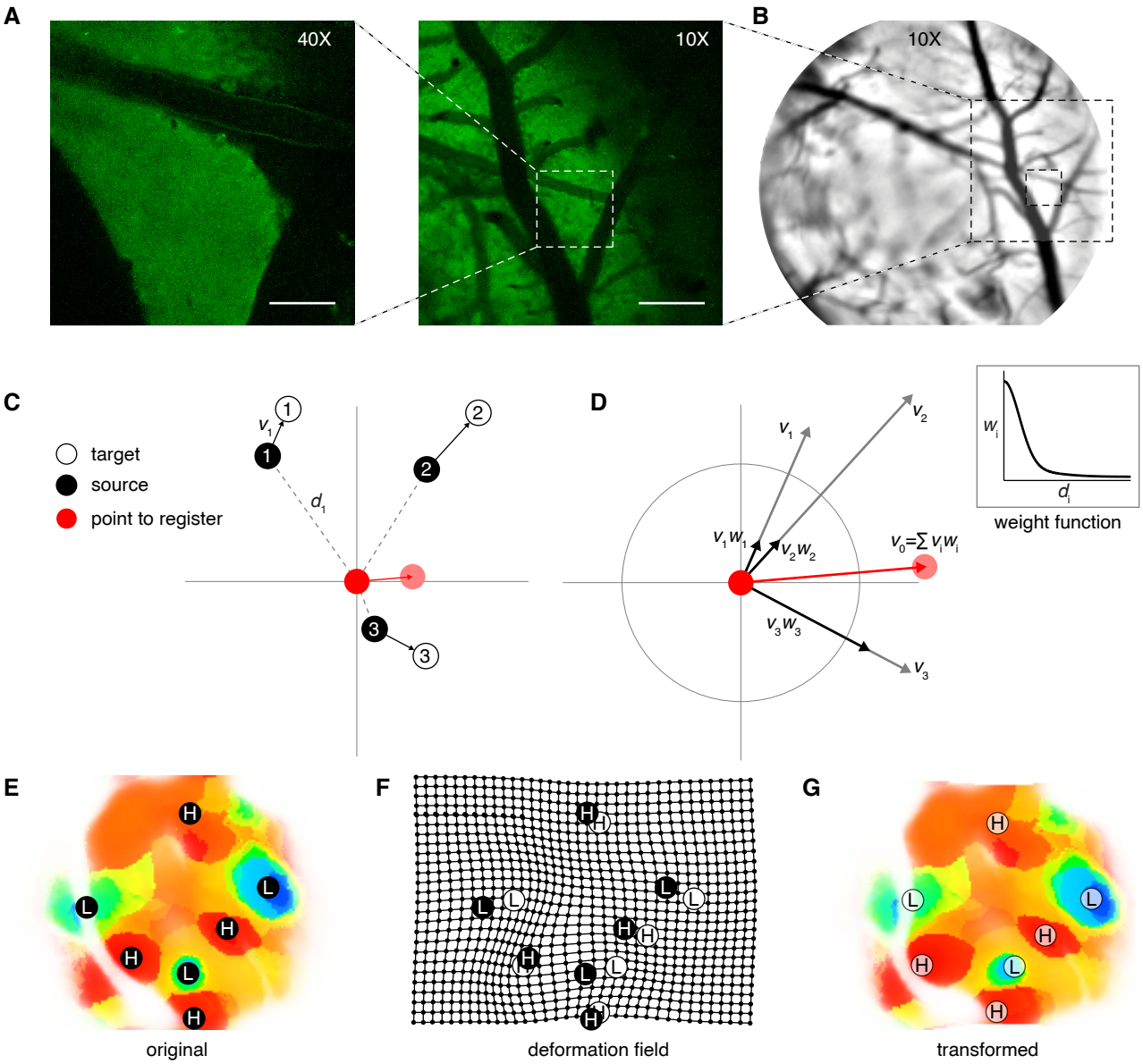
A
40X
10X
B
10X
C
target
source
point to register
D
weight function
E
original
F
deformation field
G
transformed

Figure S5. Registration of imaging fields, related to Figures 2, 6, and 7

(A-B) Registration of two-photon imaging fields onto transcranial maps. After imaging layer II/III neurons under two-photon, we focused up to the dura and obtained images at 40× and 10× magnification (A; scale bars, 50 and 200 μm). These were then compared to a baseline fluorescence image obtained transcranially (B, identical to Figure 1B). Based on the vasculature, images could be registered across different imaging modalities and magnifications, as delineated by the dotted squares.

(C-D) Radial basis function method. In this schematic, a set of three landmarks are known in both source space (filled circles) and in target space (open circles). We have a fourth point in source space, shown in red, whose position in target space is unknown. We wish to register its position in target space based on an estimate of the underlying deformation field derived from the positions of source and target landmarks. This estimation is achieved using the RBF registration algorithm detailed in Experimental Procedures. Briefly, displacement vectors $\mathbf{v}_i$ are calculated between each pair of landmark points (C, black lines; D, gray lines), and distance scalars d_i are calculated between the point to register and each source landmark (C, dashed gray lines). This distance is used to weight the contribution of each displacement vector, found by the weighting function $w_i(d_i)$ (D, inset), allowing each $\mathbf{v}_i w_i$ (D, black lines) to be computed. Finally, the weighted sum v_0 is found (D, red arrow), which indicates the estimated position of our point in target space (light red circle).

(E-G) RBF registration algorithm applied to a transcranial map. We wish to register an entire map onto a new coordinate system based on landmark positions. The original map (E) is M7 from Figure 2D, and the target landmarks are taken from M1 in Figure 2B. Using the same procedure outlined in C-D, estimated displacement vectors are calculated for each pixel in our image, generating a deformation field, as shown in F, which can then be applied to our original map to generate a transformed map (G) that is now registered to the target set of landmarks.

Figure S6

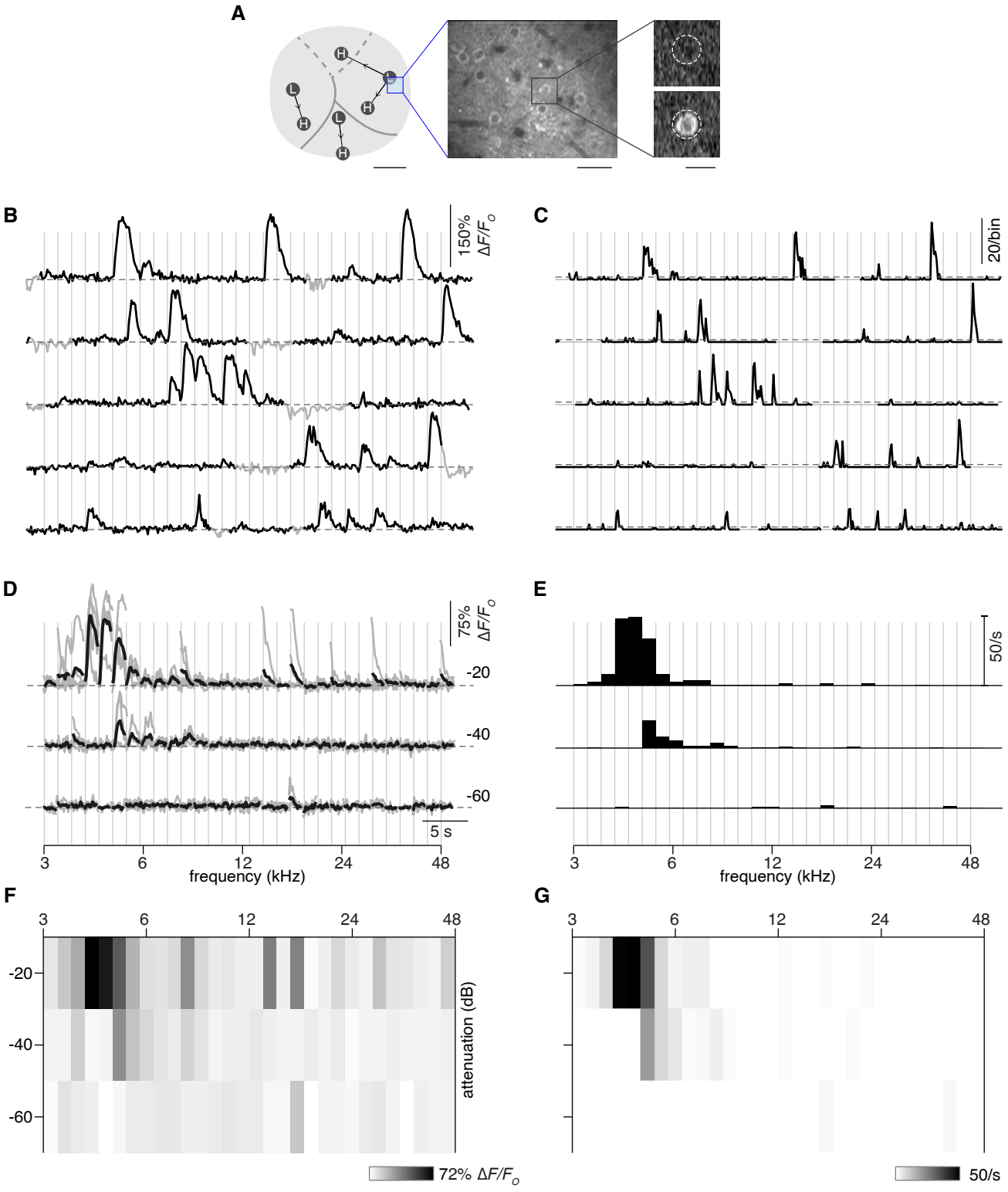
A
B
150%
ΔF/F_O
C
20/bin
D
75%
ΔF/F_O
-20
-40
-60
5 s
3
6
12
24
48
frequency (kHz)
E
50/s
3
6
12
24
48
frequency (kHz)
F
3
6
12
24
48
-20
-40
-60
attenuation (dB)
72% ΔF/F_O
G
3
6
12
24
48
50/s

Figure S6. Detailed work-up of single neuron tuning under two-photon imaging, related to Figure 3

(A) Location of neuron with respect to imaging field and transcranial functional map. Same neuron as in Figure 3. Field is located in low-frequency area of AI. Panels on right show single frames from when the neuron is silent (top) and active in response to a low frequency tone (bottom).

(B) Raw fluorescence traces for this unit in response to SAM tones at -20 dB attenuation over 5 trials. Gray portions of traces indicate times where motion was detected. These portions are ignored in subsequent analysis. Random order of frequencies is different in each trial. Vertical gray lines indicate the start of each stimulus. Note the slow decay of transients, especially evident for large responses, that is still persistent at the time of the next stimulus.

(C) Deconvolved event probabilities of the corresponding traces from B. Dashed line shows threshold used to determine size of a single event. Note that now the duration of responses is greatly shortened and most return to zero before the next stimulus.

(D) Mean responses at 3 different attenuation levels after sorting individual responses by each tone in order of increasing frequency. Gray lines show individual trials; black lines show the average.

(E) Mean event rate at the same attenuation levels as in D. Events are taken as the thresholded events counts from C and are sorted in order of increasing frequency.

(F) Frequency-response area (FRA) using the raw fluorescence responses from D. While the area of peak response is evident, many frequency-level pairs show responses only because of the slow decay of a transient initiated by a previously presented tone. For a neuron with weaker tuning, these aberrations could contaminate measures of best frequency and bandwidth.

(G) FRA using the event times from E. This estimate is vastly improved over the FRA in E and permits more accurate measures of best frequency and bandwidth.

Figure S7

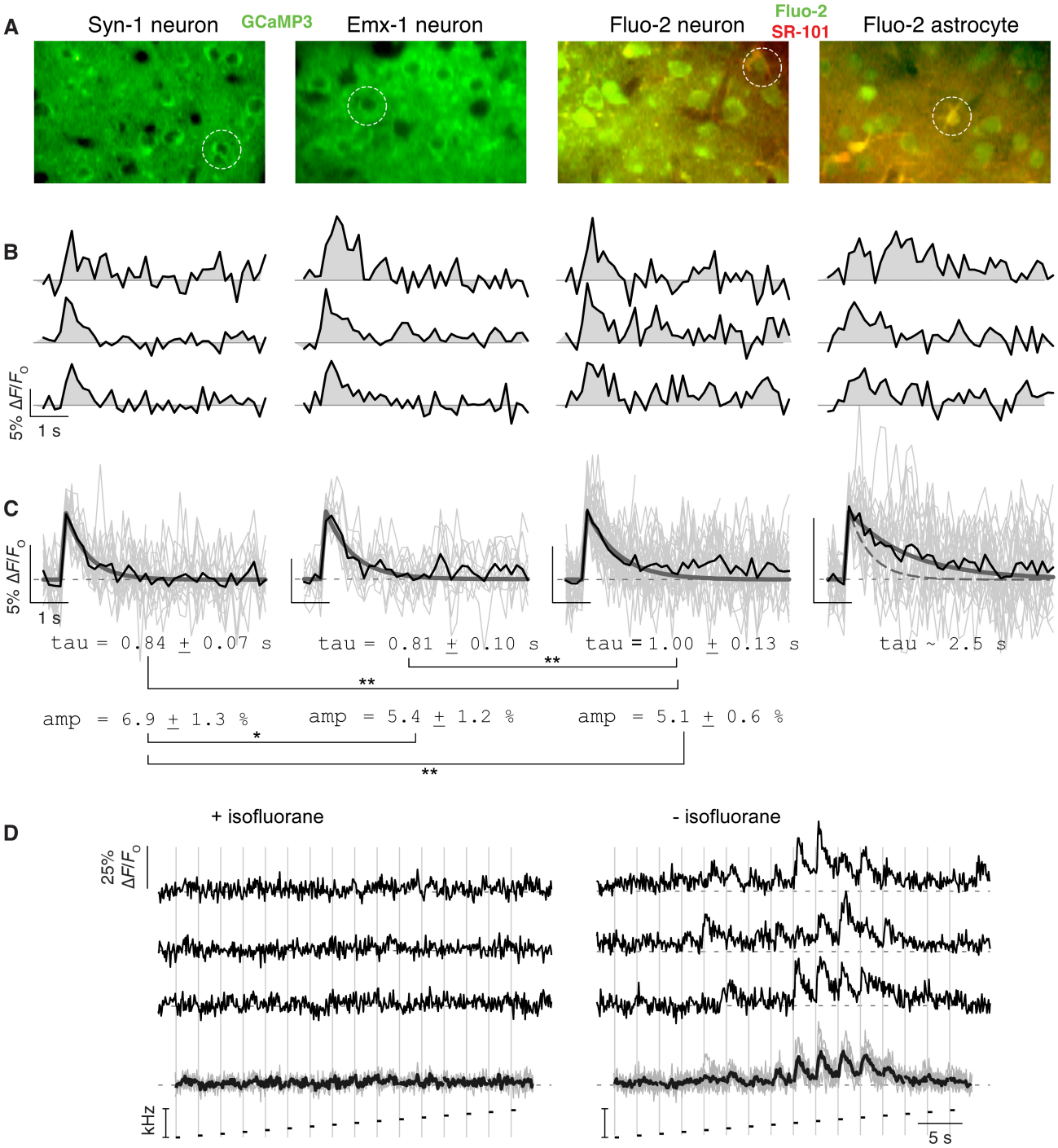
A
Syn-1 neuron
GCaMP3
Emx-1 neuron
Fluo-2 neuron
Fluo-2
SR-101
Fluo-2 astrocyte
B
5% ΔF/F0
1 s
C
5% ΔF/F0
1 s
tau = 0.84 ± 0.07 s
tau = 0.81 ± 0.10 s
tau = 1.00 ± 0.13 s
tau ~ 2.5 s
**
**
amp = 6.9 ± 1.3 %
amp = 5.4 ± 1.2 %
amp = 5.1 ± 0.6 %
*
**
D
+ isofluorane
- isofluorane
25% ΔF/F0
kHz
5 s

Figure S7. Ca^{2+} transients under different conditions, related to Figures 1-6

(A) Raw fluorescence images of GCaMP3 and Fluo-2 under two-photon imaging. In the leftmost panels, GCaMP3 fluorescence under Syn-1 and Emx-1 promoters are shown (scale bar, 25 μm). In the rightmost panels, merged images of Fluo-2 (green) and SR-101 (red) fluorescence are shown from two different experiments. Dotted white circles indicate neurons or astrocyte whose Ca^{2+} transients are subsequently shown in B-C.

(B) Examples of single transient events from neurons and astrocyte circled in A. As described in Experimental Procedures, a deconvolution algorithm detected spike probabilities, which were then converted to event times per bin by thresholding near the noise level. Bins with isolated events (2 to 5 events in a bin with no other events detected soon before or after) were chosen for averaging. Since these dyes are roughly linear for low firing rates, each event was scaled down by its magnitudes so that the transients shown are approximately single events.

(C) Average transients across all detected isolated events for neurons and astrocyte in panels A-B. Light gray traces show individual traces for each neuron or astrocyte (which include examples shown in B). Solid black trace is the average of all individual traces. Exponentials were fit to average trace using a least-squares algorithm with 4 parameters: amplitude (amp), baseline, decay time (tau), and starting time of the transient. Faster fit for Syn-1 neurons reproduced as dashed curve in Fluo-2 astrocyte trace on the far right, so as to appreciate the slower decay of astrocyte transients. GCaMP3 under either promoter was found to have significantly shorter decay times than Fluo-2 (two-sided Wilcoxon rank sum test: $p < 0.01$ indicated by **). GCaMP3 transient amplitudes for Syn-1 units was larger than for Emx-1 units or those with Fluo-2 ($p < 0.05$ indicated by *). Similar time constants for Syn-1 and Emx-1, with slower time constant in astrocytes, argues that GCaMP3 signals are mainly from neurons under both promoters. Overall in this study, 629 active GCaMP3 neurons, and 206 active Fluo-2 neurons.

(D) Effects of anesthesia on two-photon responses. Neuron activity during 1% isoflurane anesthesia (+isofluorane, left column), and 5 min after ceasing anesthesia (-isofluorane, right

column). Top 3 rows, single neuron responses to tones (increasing order, 4 to 80 kHz, 500-ms SAM tones, 2.5 s between tones). Lowest row, dark trace average. Note lack of activity and inability to resolve responses during anesthesia. While unanesthetized recordings used for actual mapping are performed >5 mins after stopping isofluorane, this example shows the drastic effects of anesthesia and recovery over even shorter time periods.
The tau and amp metrics are given as mean ±SD.

Figure S8

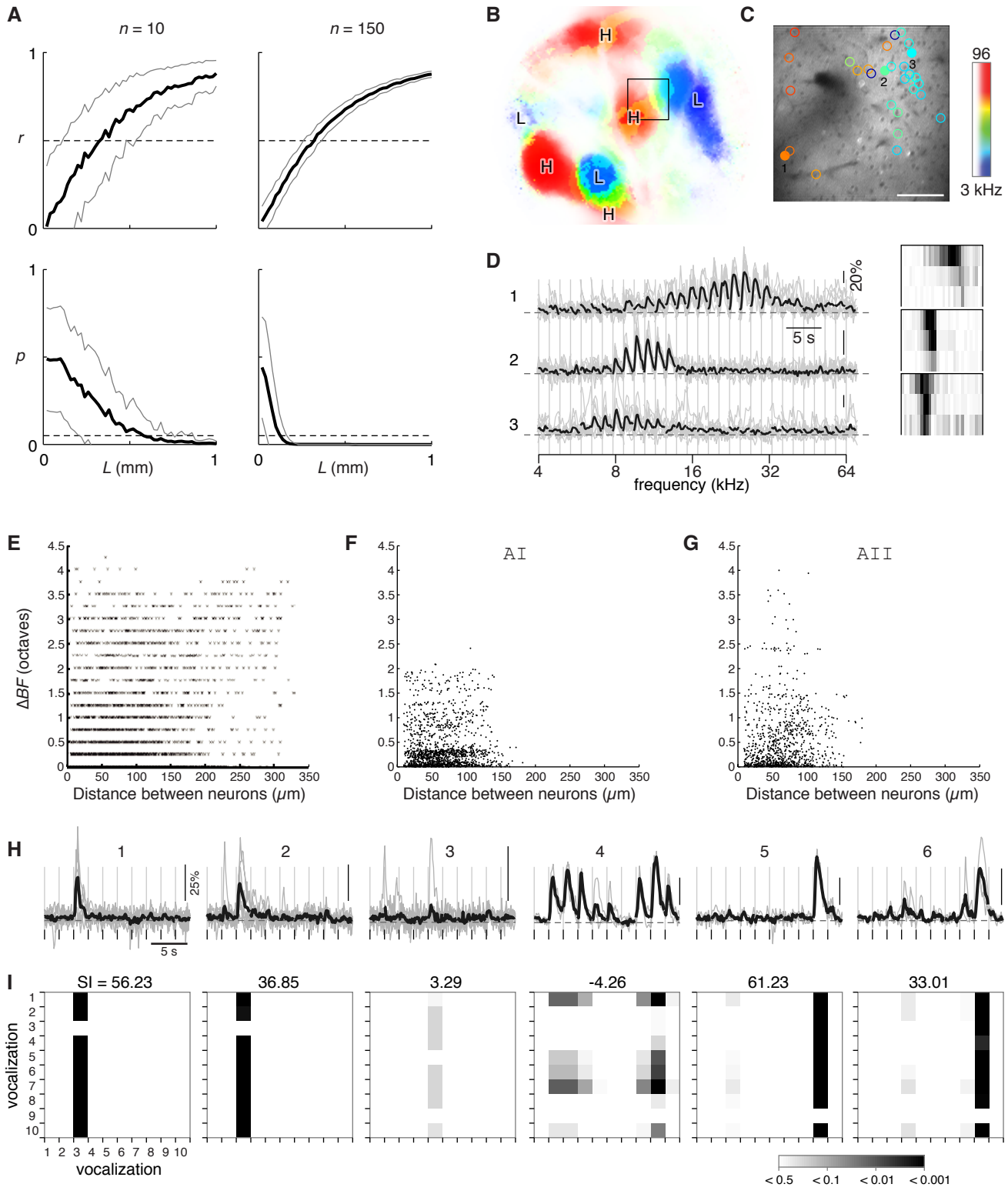
A
n = 10
n = 150
r
p
L (mm)
B
H
L
C
96
3 kHz
D
20%
5 s
frequency (kHz)
E
ΔBF (octaves)
Distance between neurons (μm)
F
AI
G
AII
H
25%
5 s
I
SI = 56.23
36.85
3.29
-4.26
61.23
33.01
vocalization
< 0.5
< 0.1
< 0.01
< 0.001

Figure S8. Co-tuning and tonotopy among neighboring neurons in present study versus prior work, related to Figures 6 and 8

(A) Simulations predicting computed correlation coefficients (*r* in top row) and correlation significance levels (*p* in bottom row), as expected for the linear relation in main text Figure 6B. The simulation incorporates: a standard deviation σ as calculated from vertical deviations of individual neurons (Figure 6B, black symbols) from the smooth regression line (black line); the number of neurons *n* within a hypothetical field of view (as labeled); and the normalized distance *L* along the main A1 tonotopic axis (as in Figure 6B) that is spanned by neurons within a field of view used to compute linear regression. A normalized length of 1 conveniently corresponds to a physical distance of ~1 mm on average. Outcomes assuming 10 neurons in the field are displayed in the left column, and those assuming 150 neurons are shown in the right column. The top row reports the predicted *r* values as a function of field size *L*, where the black curve displays the mean predicted *r* value, and the gray lines denote mean ± σ estimates of *r*. The bottom row summarizes the analogous predictions for computed *p* values, using the same format. For *n* on the order of 10, the simulation suggests that, at the typical field size of ~150 μm, one is not entitled to resolve *r* values greater than 0.5 or *p* values less than 0.05 (both shown as horizontal dashed lines in corresponding graphs). Based on this analysis, one would not resolve significant correlation until field sizes approached ~400 μm. Accordingly, we obtained a high-resolution fields of view spanning larger dimensions, as displayed in panels B-D.

(B) Transcranial map and corresponding 375 × 375 μm^2 high-resolution field of view (square). The latter is obtained with a 25× objective (Olympus XLPlan N). Mouse expressing GCaMP3 under Syn1 promoter.

(C) GCaMP3 fluorescence image obtained from mouse in panel B, using 25× objective. Tone-responsive neurons are circled, with circle color denoting best frequency. Data from this field is used for red symbols in main text Figure 6B. Clearly, a tonotopic gradient is resolved in this single larger field of view, expected from the simulations in panel A and verified by computed $r = 0.66$ and $p < 0.001$ (Pearson's analysis of 30 neurons).

(D) Ca^{2+} fluorescence responses as a function of SAM tone frequency (left) and affiliated FRAs, for three exemplar neurons labeled in panel C. Format as in main text Figure 4B.

(E) Figure 5d of Rothschild *et al* (2010) *Nature Neuroscience* is reproduced for comparison to data obtained in the present study. Plotted here is the difference in *BF* (ΔBF) versus distance between neurons (*d*) in various fields presumed to be localized to primary auditory regions. Each symbol corresponds to one neuron-to-neuron pairing.

(F) Pairwise analysis of all AI neurons in main text Figure 6B (black dots), plotted in identical format to E. ΔBF for *d* ranging between 0 to 150 μm substantiate far greater co-tuning of neurons than observed in Rothschild *et al* (2010).

(G) Pairwise analysis of all AII neurons in main text Figure 6E, plotted in identical format to E. Over the same range of *d* (0 to 150 μm), ΔBF clearly spreads to higher values than found in AI neurons in B, consistent with the analysis in main text Figure 6. Nonetheless, despite this moderate upward spread, ΔBF is still less than observed in Rothschild *et al* (2010).

(H) Single-neuron responses to vocalizations, as in bottom row of Figure 8C. Individual trials shown in gray; average of multiple trials shown in dark trace. First three columns (1-3) correspond to the same three neurons shown in Figure 8C, while the next three columns (4-6) show three neurons from a nearby field of view in the same mouse.

(I) Selectivity for vocalizations. Each subpanel displays a matrix where each pixel indicates whether the vocalization along column *i* elicits a larger response than the vocalization along row *j*. For example, the column of dark pixels for neuron 1 indicates that responses to vocalization 3 are significantly stronger than responses to other vocalizations. Color bar on bottom right indicates corresponding *p* values. Values found by applying one-way ANOVA to the responses, and then using a multiple comparison test (Tukey-Kramer method). Values atop each subpanel are the selectivity index SI, defined as $-\log(p_i)/\sum -\log(p_j), j \neq i$, where *i* is the vocalization eliciting the smallest *p*-value (p_i, summed across a column), such that neurons strongly responsive to only one vocalization will have a large SI. Across 42 neurons, mean ± σ for SI is 9.6 ± 16.7.

Table S1

	AI, current study	AII, current study	Bandyopadhyay *et al* (2010) Nature Neuroscience	Rothschild *et al* (2010) Nature Neuroscience	Hackett *et al* (2012) *Journal of Neuroscience*	Guo *et al* (2012) *Journal of Neuroscience*
Standard deviation of *BF* (across neurons in field of view)	0.405 octaves[a]	0.6195 octaves[b]	0.85 octaves (Fig. 4d legend)	see Supplemental Figure S8	-	-
r values for linear fits to *BF* versus tonotopic axis coordinate	0.88[c]	0.54[d]	0.27, 0.26, 0.17 (three individual fields)	0.76, -0.16, -0.04 (three individual fields)	0.8645	0.73 (superficial cortical layer)

[a]Averaged from 13 fields in main text Figures 6A-6B.
[b]Averaged from 16 fields in main text Figures 6D-6E.
[c]Drawn from 154 neurons in main text Figure 6B.
[d]Drawn from 143 neurons in main text Figure 6D.

Table S1. Comparing co-tuning among neighboring neurons and adherence to a tonotopic axis in present study versus that reported in Bandyopadhyay *et al* (2010) *Nature Neuroscience*, and Rothschild *et al* (2010) *Nature Neuroscience*, related to Figure 6

In regards to the extent of co-tuning among neighboring neurons within a field of view, the first row of the table calculates the standard deviation of *BF*, the metric furnished by Bandyopadhyay *et al* (2010) in their Figure 4d legend (drawn from neurons presumably localized to primary auditory regions). Our mean values are appreciably lower than reported by Bandyopadhyay *et al*, even for our AII neurons. The extent of co-tuning was compared between our study and that of Rothschild *et al* (2010) using a different metric in Supplemental Figure S8. There, we also observed greater co-tuning of neurons.

In regards to the degree to which the preferred frequencies of individual neurons adhered to a tonotopic axis, the second row of the table tabulates the correlation coefficients for linear

regressions of *BF* versus position along a tonotopic axis. Our *r* values are larger than those observed under two-photon Ca^{2+} imaging (Bandyopadhyay et al., 2010; Rothschild et al., 2010), but closely similar to those observed in prior microelectrode studies (Guo et al., 2012; Hackett et al., 2011). As the analysis in Figure S8A-D indicates, a large field of view (> 350 μm) or registration of multiple smaller fields (as in Figure 6B) is needed before significant tonotopy can be appreciated.

Online Extended Experimental Procedures

Animal Surgery and General Procedures. All animal procedures were approved by the Johns Hopkins Institutional Animal Care and Use Committee. Floxed GCaMP3 mice (R26-lsl-GCaMP3, Ai38 from Jackson Labs, JAX no. 014538) (Zariwala et al., 2012) were crossed with Syn1-Cre mice (JAX no. 003966) (Zhu et al., 2001), or Emx1-Cre mice (JAX no. 005628) (Gorski et al., 2002). Wild-type mice (C57BL/6J) were used for some of the initial crossings as well. The resultant GCaMP3-Syn1 (Syn1-Cre; R26-lsl-GCaMP3) or GCaMP3-Emx1 mice (Emx1-Cre; R26-lsl-GCaMP3) were used for experiments. Mice were anesthetized by inhaled isoflurane (1-2% in 0.5 L/min O2). Body temperature was maintained near 37ºC as measured by a rectal probe. Lidocaine (20 mg/ml) was applied topically for pain at the incision site. In some experiments, dexamethasone (up to 10 mg/kg, i.p.) was administered for inflammation and normal saline (0.5 ml, i.p.) for dehydration. Tissue overlying left auditory cortex was exposed and the skull was fixed with dental cement to a custom headpost. For transcranial imaging, the skull was thinned and kept wet with saline to increase transparency. For two-photon imaging, a 1-2 mm craniotomy was performed. In a subset of experiments, an inorganic Ca^{2+}-sensitive fluorescent dye was injected (details below).

All imaging was performed on unanesthetized mice with the head rotated ~45° about the coronal axis to bring the surface of left auditory cortex perpendicular to the microscope objective. Mice were restrained by their headpost and inside a cylinder composed of two halves of a PVC pipe taped together. They were allowed 10 or more minutes to recover from anesthesia that was used during surgery. While this amount of time may not permit full recovery from the effects of isoflurane, it did permit recovery of certain important functional parameters, such as baseline GCaMP3 activity and intrinsic fluorescence levels. Further, response properties were approximately stable over the 1 to 3 hours of each unanesthetized recording session.

Ca^{2+} Dye Injection and Cranial Window Preparation. AM ester of Fluo-2 MA (50 μg, TEFLabs) was dissolved into 4 μL of 20% Pluronic F-127 in DMSO, 0.5 μL of 2.5 mM sulforhodamine 101 (SR-101), 4 μL of 10 mM sulfinpyrazone (optional), and 54 μL of ACSF

(125 mM NaCl, 5 mM KCl, 10 mM glucose, 10 mM HEPES, 2 mM $CaCl_2$, 2 mM MgSO4), yielding a final dye concentration of ~0.75 mM. The injection pipette was filled via negative pressure and advanced to a cortical depth of 200-300 μm under two-photon visual guidance. Multiple 30-s pressure pulses (10-50 kPa) were applied. After withdrawing the pipette, the craniotomy was filled with 1.5-2% agarose (A9793, Sigma-Aldrich) and a glass coverslip (optional) was affixed on top with dental cement to dampen pulsations. Agarose and coverslip were similarly applied for non-injection experiments. Exemplar data as in Figures 4G-4I.

Widefield Transcranial Imaging of GCaMP3. Blue light illumination (460/50 nm) from an X-Cite 120Q was focused 0-200 microns below the dura through a 10× 0.25 NA objective (Olympus). Green light emission (540/50 nm) was collected by a Photometrics CoolSnap HQ camera at 20 Hz, furnishing a field of view of roughly 2×2 mm^2. Illumination power density was 0.25 mW/mm^2 and pixel size was 15×15 μm^2. In some experiments, a 4× objective was used initially to locate the extent of auditory cortex before switching to the higher power objective. Typically, however, responses to low-frequency tones provided the rostral and caudal borders and responses to high-frequency tones provided the dorsal and ventral borders of auditory cortex, and these were all contained within our 10× field of view.

We typically performed widefield imaging through a thinned skull covered by a small amount of 0.9% saline. Post-craniotomy, we rarely observed any increases in signal quality, spatial resolution, or fluorescence levels. However, if there was any amount of damage or irritation to the brain during the craniotomy, activity-dependent changes in GCaMP3 fluorescence were severely diminished or eliminated entirely, even if no swelling, bleeding, or compromise of the dura could be identified under a dissecting microscope. We observed this reduction in activity under both widefield and two-photon imaging approaches. Our impression is that GCaMP3 is exquisitely sensitive to mild inflammation that may not affect inorganic Ca^{2+} fluorescent dyes or microelectrode recordings as severely. Thus, comparison of widefield signals pre- and post-craniotomy provided an immediate functional assessment of cortical health. Finally, while removing the skull did not improve functional imaging results, fine details of the

vasculature became more apparent post-craniotomy, which in some cases aided accurate registration of fields.

Note that, with or without the skull, it was difficult to focus uniformly on the entire extent of auditory cortex, because of significant curvature (~200 μm difference in depth between central and peripheral portions of auditory cortex). However, under this one-photon mode of imaging, emitted light from a wide range of depths contributes to the signal at each pixel, corresponding to the cone of light collected above and below the chosen focal plane. Along with scatter, this large degree of signal integration was actually of benefit in dealing with curvature, as we found that responses collected at different focal depths (up to 500 μm apart) were largely indistinguishable at our level of detail.

Two-Photon Ca^{2+} Imaging. Imaging was performed using an Ultima system (Prairie Technologies) based on an Olympus BX61WI microscope. Excitation at 950 nm from a mode-locked laser (Coherent Chameleon XR Ti:Sapphire) was raster scanned at 5-12 Hz. A 40× 0.8 NA objective (Olympus) was used, yielding laser power at the sample of 20-80 mW. As noted, in some instances we instead used a 25× 1.05 NA objective (Olympus XLPlan N) to afford a larger field of view (375 μm versus 230 μm with the 40× objective). Resolution along the y-axis was reduced by a factor of 4× to allow for faster imaging, yielding a final pixel size of 0.45×1.8 μm (or 0.7×2.9 μm with the 25× objective). Dwell time was set to either 2 or 4 μs. Emission was split into red (607/45 nm) and green (525/70 nm) channels by a 575 nm dichroic mirror. The red channel was used for astrocyte detection via SR-101 (if injected), and the green channel was used for either GCaMP3 or Fluo-2 fluorescence.

Auditory Stimulation. The imaging set-up was located within a sound-attenuated room (Acoustical Solutions, Inc., AudioSeal ABSC-25) with all noise-generating equipment (computer rack, laser chiller, etc.) placed outside the room. This set-up provided roughly 40 dB of attenuation for frequencies within the mouse hearing range. During imaging sessions, mechanical shutters were disabled to prevent any additional acoustic cues. A final remaining source of sound (that could not be removed) was the galvanometers used for laser scanning. To

confirm these noise levels, we measured ambient noise along with contributions from the galvanometers using a Bruel & Kjær ¼" type 4939 microphone and a Sokolich probe (Figure S4G-H). Signals were recorded for 10 seconds and digitized at 200 kHz. Both microphones recorded noise levels of ~5 dB at 1 kHz which rolled off at –3 dB/octave to -15 dB at 100 kHz. These are noise spectrum levels in a 1-Hz band, i.e. dB *re*: 20 μPa/$Hz^{½}$ (Young and Barta, 1986), which are +10 dB (ambient noise has 10 points per 1-Hz band) above what is shown in Figure S4G-H. We found that the galvanometer, with a fundamental frequency near 600 Hz, contributed multiple peaks whose amplitudes decline at higher frequencies, as highlighted in blue in Figure S4G. This sound was constantly present and we did not appreciate significant changes in tuning over each recording session. Taken together, background ambient noise was substantially weaker than tones typically presented and, while some degree of masking may occur, this effect would be expected to be minimal.

Sounds were delivered by a free-field speaker (Tucker-Davis Technologies, ES1) placed 12 cm from the right ear. Calibration was performed with a probe tube placed at the animal's right pinna. Intensity levels were found to be flat (±15 dB) for the frequencies used (3 to 96 kHz). Stimuli consisted of sinusoidal amplitude modulated (SAM) tones (300-500 msec, 10-40 Hz modulation), pure tones (20-600 msec), and mouse vocalizations. Note that pure tones were only used for Figure S3A-B, and vocalizations were only used as indicated in Figures 7 and 8. Otherwise, only SAM tones were used. All stimuli were cosine-squared gated (1-5 msec) and typically played in a random order with 1.5-2.5 sec between onsets. A single presentation of each stimulus was sufficient for transcranial imaging (although multiple trials were often run) while 3-10 repetitions were used for two-photon imaging. Additionally, each stimulus was run at multiple attenuation levels, typically ranging from 60 dB attenuation up to 20 dB attenuation in 20 dB steps, although in some experiments more sound levels were used. Typically, 16 frequencies covering 5 octaves were used for transcranial imaging (3 frequencies per octave) while 30 frequencies covering 4 octaves were used for two-photon imaging (7.25 frequencies per

octave). Vocalizations used were taken from an online database of published adult mouse calls (Grimsley et al., 2011) and were played back with 2 sec between onsets.

Immunohistochemistry. Mice were deeply anesthetized with pentobarbital and perfused with freshly prepared 4% paraformaldehyde (PFA in 0.1M phosphate buffer). Brains were post-fixed in 4% PFA overnight at 4ºC and stored in phosphate buffered saline (1X PBS) at 4ºC until further processed. 35µm thick coronal brain sections cut with vibratome were incubated overnight with primary antibodies against GFAP (pRabbit; 1:500, DAKO), GFP (pGoat; 1:5000, Sicgen), and NeuN (mMouse; 1:500, Chemicon). After rinsing twice in 1X PBS, sections were further incubated for 2 hours at room temperature with corresponding secondary antibodies raised in donkey: Alexa-488, Alexa-546, and Alexa-647 (1:2000, Life Technologies or Abcam). Finally sections were rinsed thrice in 1X PBS at room temperature and mounted on superfrost glass slides using Aqua Polymount (Polysciences, Inc.). Z-stack images of stained sections were obtained using a Zeiss laser scanning confocal microscope (Zeiss, 510 Meta) at a resolution of either 0.82 µm with a 25× objective or 0.33 µm with a 63× objective. All images were processed with Fiji or ImageJ (NIH) (Agarwal et al., 2012).

Data Analysis. Multiple processing steps were applied on our imaging data, with analysis falling within the following categories: transcranial image analysis, two-photon image analysis, registration, and response metrics. These are described in detail below. All analysis was carried out in ImageJ (NIH) and MATLAB (MathWorks).

Transcranial Image Analysis. Three main issues arise here: intensity across the imaging field is inhomogeneous, baseline fluorescence fluctuates over time, and the spatial resolution is decreased by tissue scattering. These issues are addressed sequentially as follows.

Image Normalization. To correct for inhomogeneities in our imaging field due to nonuniformity in illumination and emission we normalized the fluorescence data by calculating the mean image intensity across time for each pixel, spatial low-pass filtering the mean intensity image with a Gaussian filter, and then normalizing each frame of the fluorescence time series by the filtered mean intensity image.

Structured Sparse Encoding Algorithm. To extract meaningful calcium transient events and spatial regions corresponding to those events, we employed a structured sparse encoding algorithm (Haeffele et al., 2014). Let $I \in \mathbb{R}^{TxMN}$ denote the normalized fluorescence data where each column of I contains the time series for a single pixel. Here T denotes the number of time points in the recording and the image size is $M \times N$ (pixels). In this algorithm, the normalized image I is assumed to be of the following form:

$$I = DX_s + BX_B + \eta$$

where D is a dictionary representing the temporal dynamics of a calcium transient, X_s is a matrix containing the estimated spiking activity for each pixel, B is a dictionary of low frequency Fourier components to fit slow variations in the baseline of our movie over time, X_B contains the baseline fit parameters for each pixel, and η represents noise ($\eta \sim N(0,\sigma^2)$). We assume calcium transients are decaying exponentials, and the columns of D are given by:

$$d_i(t) = e^{-(t-it_s)/\tau}u(t - it_s)$$

where $d_i(t)$ denotes the i^{th} column of D, $u(t)$ is the unit step function, t_s is the sampling period, and τ is a decay constant (set at 0.5 sec). We then optimized the least-squares fit of the model to the normalized images while convexly regularizing X_S and X_B to be simultaneously sparse, low-rank, and having small variation between neighboring pixels. The fit of X_s is used for subsequent analysis. In particular, we take the average value of X_s at each pixel over a 400 ms window after the onset of each stimulus to measure the response to a given stimulus at that pixel.

The model fit was validated by considering whether the error $E = I - DX_s - BX_B$ was normally distributed, as expected if η is Gaussian noise. We performed a Shapiro-Wilk test on each pixel and calculated the p value. At a significance level of 0.05, 93.59% of pixels passed the test for normality, indicating the residual of our fit was likely expected Gaussian noise. Further, fits were validated by inspecting brightness-over-time fits at randomly chosen pixels or regions.

Deblurring. Imaging of neural activity in cortex, especially of deeper layers, comes with a large degree of blur due to light scatter. This scatter limits spatial resolution of single-photon imaging on the order of 200 μm (Orbach and Cohen, 1983). We deblurred our spatial response maps with

the Lucy-Richardson deconvolution (Lucy, 1974; Richardson, 1972) (Figure S3). Our point spread function was specified as a Gaussian with width $\sigma = 200$ μm.

Two-Photon Image Analysis. For two-photon imaging, cells were manually circled to delineate regions-of-interest (ROIs). These were then used to generate brightness-over-times (BOTs) for each cell. All pixels within each ROI were weighted equally. To account for slow drift, ROIs were adjusted on a trial-by-trial basis. However, within a trial, we assumed a stable baseline, which was found by an iterative method as follows: 1) measure mean and standard deviation of the trace, 2) remove any data points more than 1.5 standard deviations from the norm, 3) repeat. At this point, any features of our image that resembled a cell or showed any transient activity were circled. These initial criteria were intended to be generous. However, for further analysis, we manually eliminated any cells that either showed no transients in any trial or whose fluorescence fluctuated significantly over slow timescales (indicative of astrocyte activity or high firing rate neurons that are not amenable to interpretation).

Next a non-negative deconvolution method was applied to generate spike probabilities (Vogelstein et al., 2010), which were then thresholded to estimate event times or, more precisely, events per time bin. This statistic (events per time bin) was then used to calculate tuning curves. The advantage of such an approach is two-fold. First, noise and baseline fluctuations are greatly suppressed as they tend to be ignored by the deconvolution and the thresholding. Second, the responses are temporally sharpened by the deconvolution. A transient response can last for over a second and run into subsequent stimulus presentation, whereas in practice the deconvolved estimate is normally limited to a few hundred milliseconds (Figure S6).

Registration. Registration was a multi-step process (see Figure S5). We acquired transcranial responses to tones for each mouse, which provided us with a functional map and an anatomical vasculature map. Then, after imaging each field-of-view under two-photon, we focused up to the dura, where we acquired images of the surface vasculature at both 10× and 40× magnifications (Figure S5A). We also utilized the change in focal depth to estimate the depth of our fields (reported in Figure S1Q). For experiments where we injected Fluo-2 AM, we could, at 10×, also

see increased green fluorescence at the location of the dye injection. Vasculature was prominent under all imaging modalities and thus allowed us to register each individual two-photon field-of-view to that animal's transcranial map (Figure S5B). Next, we wished to register field-of-views across animals based on functional landmarks. Because the precise functional map varies across animals in a non-rigid manner, we performed local, elastic registration. Specifically, since the most robust features were peak activation areas at low and high frequencies, we used a landmark-based radial-basis function (RBF) method.

RBF registration algorithm. To place imaging sessions from different animals on different days on a single map, we registered each experiment onto a single canonical map. This registration was based on the 7 landmarks identified as fiduciaries (3 at low frequency and 4 at high frequency areas). To perform local, elastic registration, we employed a version of a landmark-based radial basis function method (Arad and Reisfeld, 1995; Cavoretto et al., 2011). For each pair of landmarks, a displacement vector is calculated and its contribution to the final registration is weighted by a radial basis function that depends only on the distance to the point being registered. An example using 3 landmarks is illustrated in Figures S5C and S5D.

In particular, let $\mathbf{s}_i$ and $\mathbf{t}_i$ be our landmarks in source and target space, respectively, for each of the 7 landmarks ($i = 1, \cdots, 7$). We wish to register a point $\mathbf{p}$ in source space to a point $\bar{\mathbf{p}}$ in target space. For each landmark, we calculate a displacement vector $\mathbf{v}_i = \mathbf{t}_i - \mathbf{s}_i$ between target and source landmarks and a distance $d_i = \|\mathbf{p} - \mathbf{s}_i\|$ from the point $\mathbf{p}$ to each source landmark, where $\|\bullet\|$ is the Euclidean norm. Then we find $\bar{\mathbf{p}}$ by the following weighted sum:

$$\bar{\mathbf{p}} = \mathbf{p} + \frac{1}{\xi}\sum_{i=1}^{7} \mathbf{v}_i w(d_i)$$

The weighting $w(d_i)$ is a radial basis function (Figure S5D, inset) that, in our implementation, takes the following form:

$$w(d_i) = k_0 + k_1 e^{-(d_i/\sigma_1)^2} + e^{-(d_i/\sigma_2)^2}$$

Thus $w(d_i)$ is a sum of Gaussians (with widths σ_1 and σ_2) and relative contributions determined by k_1 and a constant k_0 (for global support). The scalar $\xi = \sum w(d_i)$ is a normalization factor.

Values were chosen based on empirical considerations. We used $k_0 = 0.01$, $k_1 = 0.1$, $\sigma_1 = 0.75$ mm, and $\sigma_2 = 0.3$ mm. This algorithm was used to register our transcranial maps onto a common set of landmarks as briefly illustrated in Figure S5E-G.

Response Metrics. Before calculating any response measures, motion was semi-automatically detected by looking for periods of large and rapid deviations from the mean intensity. These frames were then ignored in any further analysis. We measured average responses over periods of 400-600 ms after the start of each stimulus.

For transcranial imaging, we first selected field-wide 'global thresholds' at each frequency presented (as shown by the jagged thin black line in Figure 2A). We used this threshold to calculate a preferred frequency f_{pref} at each pixel location. This calculation was performed by taking the weighted average of the three frequencies that elicited the largest responses at that pixel. If frequencies f_1, f_2, and f_3 elicit the largest responses r_1, r_2, and r_3, then

$$f_{\text{pref}} = (r_1 \cdot f_1 + r_2 \cdot f_2 + r_3 \cdot f_3) / (r_1 + r_2 + r_3)$$

where frequencies here are on a logarithmic scale. The final preferred frequency in Hz can be recovered by reversing the logarithm.

For whole-field FRAs, we calculated thresholds by first averaging the response across all pixels for each level-frequency combination. Next, we applied a 5-point Gaussian filter (sigma of 1) to smooth the data. Then, at each frequency, we linearly interpolated to find the sound level that provides a half-maximum response. For frequencies that never exceeded half-max, we assigned a threshold of +20 dB attenuation. For frequencies that exceeded half-max at even the lowest sound level tested, we assigned a threshold 10 dB lower than the minimum tested. Attenuations were converted to dB SPL using our probe tube calibration.

For two-photon imaging, we deemed neurons to be tone responsive if, under any tone stimulus, neuronal outputs surpassed baseline by at least one standard deviation plus an average of 5 events per second. While these strict criteria potentially eliminated neurons with weak activity and high noise levels, they served to filter out unreliable data and neurons whose signals were contaminated by signal spillover from neuropil. Given these criteria, the overall data set

was as follows. In AI, 662 cells were manually circled, 402 of those were active and had stable baselines, and 154 were responsive to tones. In AII, the numbers were 745/433/143. Thus, in both fields, roughly a third of active neurons were tone responsive (38.3% in AI; 33.0% in AII). This proportion is similar to that found in a prior two-photon study using an inorganic chemical fluorescent dye, wherein 376 neurons (42%) were tone-selective, out of a pool of 895 neurons exhibiting Ca^{2+} transients (Rothschild et al., 2010). Note that, loosening our criteria such that > 50% of active neurons would be included as tone responsive did not change the results of statistical tests applied to our population data (as in Figure 6 and Table S1).

Threshold was chosen as the lowest sound level at which a significant response was found. At that threshold, best frequency was chosen as the optimal frequency. Three approaches were used: 1) the mean of a fitted Gaussian, 2) the weighted average of all significant responses, and 3) the peak response. Although they usually yielded similar results, for robustness we defined best frequency as the median of these measures.

Next, we defined bandwidth at each sound level as the average of 1) the width of a fitted Gaussian at half-maximum and 2) the range of frequencies that elicited a response greater than half-maximum. Because we used a limited number of sound levels, it was not normally possible to choose a well-behaved $Q10$ or $Q40$. Instead, we opted to use whatever sound level had the largest bandwidth; thus, Q was defined as best frequency at the threshold sound level divided by the maximum bandwidth at any sound level.

Population FRAs were taken as the average firing rate (events per second) of all neurons in that field. For any population measures, only cells with a significant response for at least one sound level and frequency were included. ‘BF spread’ (ΔBF) was defined as the absolute difference in best frequency for each pair of tone-responsive neurons in a field, measured in octaves.

Supplemental References

Agarwal, A., Dibaj, P., Kassmann, C.M., Goebbels, S., Nave, K.A., and Schwab, M.H. (2012). In vivo imaging and noninvasive ablation of pyramidal neurons in adult NEX-CreERT2 mice. Cereb Cortex 22, 1473-1486.

Arad, N., and Reisfeld, D. (1995). Image warping using few ahchor points and radial functions. Computer Graphics Forum 14, 35-46.

Bandyopadhyay, S., Shamma, S.A., and Kanold, P.O. (2010). Dichotomy of functional organization in the mouse auditory cortex. Nat Neurosci 13, 361-368.

Cavoretto, R., De Rossi, A., and Quatember, B. (2011). Landmark-based registration using a local radial basis function transformation. Journal of numerical analysis, industrial, and applied mathematics 5, 141-152.

Gorski, J.A., Talley, T., Qiu, M., Puelles, L., Rubenstein, J.L., and Jones, K.R. (2002). Cortical excitatory neurons and glia, but not GABAergic neurons, are produced in the Emx1-expressing lineage. J Neurosci 22, 6309-6314.

Grimsley, J.M., Monaghan, J.J., and Wenstrup, J.J. (2011). Development of social vocalizations in mice. PLoS ONE 6, e17460.

Guo, W., Chambers, A.R., Darrow, K.N., Hancock, K.E., Shinn-Cunningham, B.G., and Polley, D.B. (2012). Robustness of cortical topography across fields, laminae, anesthetic states, and neurophysiological signal types. J Neurosci 32, 9159-9172.

Hackett, T.A., Barkat, T.R., O'Brien, B.M., Hensch, T.K., and Polley, D.B. (2011). Linking topography to tonotopy in the mouse auditory thalamocortical circuit. J Neurosci 31, 2983-2995.

Haeffele, B.D., Young, E.D., and Vidal, R. (2014). Structured Low-Rank Matrix Factorization: Optimality, Algorithm, and Applications to Image Processing. In Proceedings of The 31st International Conference on Machine Learning (Beijing, China).

Lucy, L.B. (1974). An iterative technique for the rectification of observed distributions. Astronomical Journal 79, 745.

Orbach, H.S., and Cohen, L.B. (1983). Optical monitoring of activity from many areas of the in vitro and in vivo salamander olfactory bulb: a new method for studying functional organization in the vertebrate central nervous system. J Neurosci 3, 2251-2262.

Richardson, W.H. (1972). Bayesian-based iterative method of image resotration. J Opt Soc Am 62, 55-59.

Rothschild, G., Nelken, I., and Mizrahi, A. (2010). Functional organization and population dynamics in the mouse primary auditory cortex. Nat Neurosci 13, 353-360.

Vogelstein, J.T., Packer, A.M., Machado, T.A., Sippy, T., Babadi, B., Yuste, R., and Paninski, L. (2010). Fast nonnegative deconvolution for spike train inference from population calcium imaging. J Neurophysiol 104, 3691-3704.

Young, E.D., and Barta, P.E. (1986). Rate responses of auditory nerve fibers to tones in noise near masked threshold. J Acoust Soc Am 79, 426-442.

Zariwala, H.A., Borghuis, B.G., Hoogland, T.M., Madisen, L., Tian, L., De Zeeuw, C.I., Zeng, H., Looger, L.L., Svoboda, K., and Chen, T.W. (2012). A Cre-dependent GCaMP3 reporter mouse for neuronal imaging in vivo. J Neurosci 32, 3131-3141.

Zhu, Y., Romero, M.I., Ghosh, P., Ye, Z., Charnay, P., Rushing, E.J., Marth, J.D., and Parada, L.F. (2001). Ablation of NF1 function in neurons induces abnormal development of cerebral cortex and reactive gliosis in the brain. Genes Dev 15, 859-876.